ELSEVIER

Contents lists available at ScienceDirect

## Applied Catalysis B: Environmental

journal homepage: www.elsevier.com/locate/apcatb





# *In-situ* exsolution of bimetallic CoFe nanoparticles on (La,Sr)FeO<sub>3</sub> perovskite: Its effect on electrocatalytic oxidative coupling of methane

Jaesung Kim<sup>a</sup>, Yu Jin Kim<sup>b</sup>, Matthew Ferree<sup>a</sup>, Seval Gunduz<sup>a</sup>, Anne C. Co<sup>c</sup>, Minkyu Kim<sup>\*,b</sup>, Umit S. Ozkan<sup>a,\*</sup>

- a William G. Lowrie Department of Chemical and Biomolecular Engineering, The Ohio State University, Columbus, Ohio 43210, United States
- <sup>b</sup> School of Chemical Engineering, Yeungnam University, Gyeongsan, Gyeongbuk 38541, Republic of Korea
- <sup>c</sup> Department of Chemistry and Biochemistry, The Ohio State University, Columbus, Ohio 43210, United States

#### ARTICLE INFO

# Keywords: Oxidative coupling of methane Solid oxide cell Exsolution Perovskite

#### ABSTRACT

This study presents in-situ reduction of lanthanum strontium cobalt ferrite (LSCF) perovskite as an effective method for modifying its surface properties and enhancing its electrocatalytic reactivity for oxidative coupling of methane (OCM). The evolution of hetero-phases during the reduction of LSCF resulted in CoFe nanoparticles being formed at the surface. The in-situ reduced LSCF cell for OCM could be operated in either an ion pump or a fuel cell mode. High selectivity of 63% and 10.2% were reported for  $C_{2+}$  hydrocarbons and  $C_3H_6$ , respectively. DFT calculations on LSCF and CoFe revealed that the high selectivity of  $C_{2+}$  hydrocarbons on the LSCF primarily stems from the presence of CoFe nanoparticles. In-situ DRIFTS conducted under  $CH_4$  proved that complete oxidation of  $CH_4$  can be effectively inhibited by reducing LSCF, and control of oxygen supply is an important parameter for selective conversion of  $CH_4$  to higher order hydrocarbon.

#### 1. Introduction

In recent decades, technology has greatly advanced the refinement of shale gas, which produces abundant methane [1]. Methane is a small and stable molecule characterized by strong C–H bonds (439.3 kJ mol<sup>-1</sup>), negligible electron affinity, large ionization energy, and low polarizability [2]. In order to convert methane into chemicals, such as alcohols and olefins, a steam reforming reaction is typically involved, which is an endothermic and inefficient process. As an alternative, it may be more efficient to eliminate the reforming step from the process and convert methane directly into valuable compounds.

In a heterogeneous catalysis process, it is possible to perform the direct conversion of methane either by non-oxidative or oxidative coupling [2]. During oxidative coupling of methane (OCM), CH<sub>4</sub> undergoes partial oxidation, leading to the formation of an unpaired methyl radical (CH<sub>3</sub>•), which couples with another methyl radical to form  $C_2H_6$  (Eq. 1). The reaction may continue by a subsequent oxidative dehydrogenation of  $C_2H_6$  (Eq. 2), thus releasing  $C_2H_4$ [3].

$$2CH_4 + \frac{1}{2}O_2 \rightarrow CH_3CH_3 + H_2O, \tag{1}$$

$$\Delta H_{298K} = -87.8 \text{ kJ mol}^{-1}$$

$$2CH_4 + O_2 \rightarrow CH_2CH_2 + 2H_2O, 
\Delta H_{298K} = -140.4 \ kJ \ mol^{-1}$$
(2)

$$CH_4 + O_2 \rightarrow CO_2 + 2H_2O,$$
  
 $\Delta H_{298K} = -801.3 \ kJ \ mol^{-1}$ 
(3)

Recent years have seen significant research efforts, seeking out catalysts that can maximize the yield of  $C_2$  hydrocarbons, such as ethane and ethylene. Based on the evidence thus far, however, it has been suggested that the low yields of  $C_2$  hydrocarbons is due to the rate of hydrogen abstraction from  $C_2$  products being greater than the rate of hydrogen abstraction from methane on most heterogeneous catalysts [4]. A kinetic study has predicted that catalytic processes for OCM can yield  $C_2$  hydrocarbons up to an upper limit of 28–30% [5].

In light of this, other approaches need to be considered for OCM. The yields to  $C_2$  hydrocarbons follow a half-order dependence on  $O_2$  partial pressure while deep oxidation of  $CH_4$  to CO and  $CO_2$  shows first-order dependence (Eq. 3) [6]. As such, one strategy to improve the  $C_2$ 

E-mail addresses: mk\_kim@ynu.ac.kr (M. Kim), ozkan.1@osu.edu (U.S. Ozkan).

<sup>\*</sup> Corresponding authors.

selectivity is to use a membrane reactor able to operate OCM at low partial pressure of oxygen. Particularly, solid oxide cells (SOCs) consisting of solid oxide electrolyte membrane and electrodes that are able to regulate oxygen ion flux based on fine control of appropriate current. SOCs are a doubly attractive option because of the additional valuable products that can be generated on the cathode depending on the reaction of choice, such as the electrolysis of H<sub>2</sub>O or CO<sub>2</sub>, while performing OCM at the anode [7]. A further advantage of SOCs is that electricity can be spontaneously generated during OCM. Even with these advantages, OCM using SOC is still challenging since most high temperature catalysts have mixed ionic and electronic conductivity that chemically drives CH<sub>4</sub> to CO and CO<sub>2</sub> [7–9].

In our previous work, the exsolved B-site metal nanoparticles on the perovskite surface induced by exposing it to H2 atmosphere was recognized as an important factor for the improvement of electrocatalytic activity for CO<sub>2</sub> electrolysis [10]. It is reasonable to expect that the exsolution of B-site atoms could be triggered by the exposure of the perovskite to other reducing gases such as CO or hydrocarbons. It is for this reason that an in-situ reduction of an anode would be feasible, resulting in the modification of its surface characteristics which lead to enhanced electrocatalytic activity, during the oxidation reaction of hydrocarbons. In this study, we hypothesized that the catalytic properties of the perovskite oxide surface can be modified by exposing it to CH<sub>4</sub> gas. We explored La<sub>0.7</sub>Sr<sub>0.2</sub>Co<sub>0.2</sub>Fe<sub>0.8</sub>O<sub>3</sub> (LSCF) catalyst as an anode in a solid oxide cell working either in fuel cell or ion pump mode for OCM to produce ethylene and propylene. The in-situ exsolution of bimetallic CoFe nanoparticles and the resulting improvement in electrocatalytic performance of LSCF anode for OCM were verified by surface and bulk analysis. DFT calculations were also conducted to confirm the selective OCM reaction pathways on the exsolved CoFe nanoparticles and the surface of LSCF by examining the various active sites.

#### 2. Experimental section

#### 2.1. Preparation of catalysts

A citric acid-ethylenediaminetetraacetic acid (EDTA) complexation method was used to synthesize A-site deficient Sr and Co doped lanthanum ferrite perovskite, La $_{0.7}$ Sr $_{0.2}$ Co $_{0.2}$ Fe $_{0.8}$ O $_{3}$  (LSCF), as reported in our earlier publication [11]. Reduced LSCF samples (Red-LSCF) were prepared by reducing the calcined LSCF powders under 5% H $_{2}$ /N $_{2}$  at 850 °C.

#### 2.2. Evaluation of electrocatalytic performance

A screen-printing technique was used to make electrocatalytic button cells on commercial Yttria-stabilized zirconia (YSZ) electrolyte (25 mm diameter, 125 µm thickness, Nextech Materials). On the anode side, a gadolinium doped ceria (GDC) interlayer was printed and sintered at 1400  $^{\circ}$ C for 2 h under N<sub>2</sub> flow. LSCF mixed with GDC at 40 wt% was printed with 0.72 cm<sup>2</sup> on the GDC layer and sintered at 1200 °C under air. A cathode side LSM-YSZ layer was printed and sintered at 1200  $^{\circ}\text{C}$ under air. The gold wire was applied to the electrodes with the use of gold paste. In the electrocatalytic performance tests, pure CH<sub>4</sub> (99.99%), flowed to the anode side at a rate of 10 sccm and experiments were performed at 800 °C, 825 °C, and 850 °C. The electrochemical impedance spectra (EIS) were collected in the frequency range from 1 MHz to 10 mHz. The equivalent circuit model of  $R_S(R_{P1}Q_1)(R_{P2}Q_2)$  was used consisting of an ohmic resistance (Rs) and two contributions to polarization impedance  $(R_P)$  and constant phase elements (Q) in parallel. Quantification of the gas products was performed on an on-line gas chromatograph (Shimadzu 2014) equipped with a pulse discharge ionization detector (PDHID) and a flame ionization detector (FID).

#### 2.3. Characterizations

The analysis of X-ray diffraction patterns of the catalysts were performed on a Bruker D8 Lead X-ray powder diffractometer equipped with a Cu K $\alpha$  X-ray source. In the generator, the voltage was 40 kV and the current was 40 mA. Scans were performed in a  $2\theta$  range of  $20\text{--}60^\circ$ , and the step size was set at  $0.014^\circ$  per 0.5 s. Phase identification was done using the crystallographic open database (COD). Rietveld refinement was used to calculate Miller indices from the XRD patterns using General Structure Analysis System-2 (GSAS-2) software [12]. The extent of exsolution,  $\xi$ , was calculated as the ratio of moles of CoFe to moles of the parent perovskite based on the refined mass fraction [13]. Crystal structures were visualized by VESTA [14]. In-situ XRD required the use of an Anton Paar HTK1200 oven at various temperatures from 30 °C to 800 °C.

The Raman spectra were obtained with a Horiba LabRAM HR-800 Raman Spectrometer equipped with an asymmetric Czerny Turner spectrometer (1200 g mm $^{-1}$  grating) and a CCD detector (1024  $\times$  256 pixels, each pixel measuring 26  $\mu m$   $\times$  26  $\mu m$ ). Five scans were taken over an exposure time of 60 s to collect the spectrum.

Analysis of the surface elemental oxidation state and composition was carried out by X-ray photoelectron Spectroscopy (XPS) using a Kratos Axis Ultra XPS instrument equipped with a monochromated Al K $\alpha$  X-ray source (1254 eV, 12 kV, 10 mA) and a charge neutralizer at 2.05 A of element current, 1.3 V of filament bias, and 3.6 V of charge balance. C 1 s standard peak at 284.5 eV was used for calibration for each scan. 8 sweeps of high-resolution scans for La 3d, Sr 3d, Co 2p, and Fe 2p were performed with a 450 ms dwell time in the narrowed binding energy ranges.

X-ray Absorption Near Edge Spectroscopy (XANES) was conducted at Sector 10-BM of the Materials Research Collaborative Access Team (MRCAT) at the Advanced Photon Source (APS, Argonne National Laboratory). The instrument was operated in transmission mode for all samples. The catalyst powders were diluted with boron nitride in a ratio of 1:5. The Fe K-edge and Co K-edge were scanned at 7112 eV and 7717 eV, respectively, for both catalyst samples. The corresponding metal foils were used as references to calibrate the K-edge spectra. Athena software was utilized to process the collected data [15].

The scanning transmission electron microscope (STEM) was used for an investigation of LSCF and Red-LSCF using a TECNAI F20 TEM operating at 200 kV equipped with an energy dispersive X-ray spectroscopy (EDS).

Diffuse reflectance infrared Fourier transform spectroscopy (DRIFTS) data were collected using Thermoelectron Nicolet 6700 FTIR equipped with an MCT detector. Powder samples were diluted with potassium bromide (KBr) in a 1:20 ratio of catalyst to KBr. For in-situ DIRFTS under CH<sub>4</sub>, the DRIFTS spectra of the pretreated samples were acquired under 30 sccm of 10% CH<sub>4</sub>/He at 450 °C. For temperature-programmed desorption (TPD) -DRIFTS, the samples were pretreated with helium at 450 °C to desorb any additional adsorbed species. The samples were exposed to CO<sub>2</sub> at 50 °C and DRIFTS spectra was collected at various temperatures under helium.

For temperature-programmed reduction/oxidation (TPR/TPO), 30 sccm of gas mixture was flowed through 50 mg of catalyst powders and the effluence was analyzed by an MKS Cirrus mass spectrometer.  $5\%~H_2/N_2$  was used for TPR and  $2\%~O_2/He$  or  $5\%~CO_2/He$  was for TPO. The reactor was heated from room temperature to  $1000~^{\circ}\text{C}$  with a ramp rate of  $10~^{\circ}\text{C}$  min $^{-1}$ .

For measurement of electrical conductivity, we prepared the sample pellets by compressing the powder in a hydraulic press, followed by sintering at 1300  $^{\circ}$ C for 5 h. A gold paste was used to connect four gold wires to four points on the pellet. The two leads with current application were connected to Keithley 6220 current source. The two leads with voltage measurement were connected to Keithley 6182 sensitive nanovoltmeter.

#### 2.4. Computational details

All plane wave DFT calculations were performed using the projector augmented wave pseudopotentials provided in the Vienna ab initio simulation package (VASP) [16,17]. The spin polarized Perdew-Burke-Ernzerhof (PBE) exchange-correlation with Hubbard U corrections S were used with a plane wave expansion cutoff of 400 eV. U corrections were only applied for LSCF structure with the 4 eV on Co and F [18]. We had replaced La and Fe of LaFeO<sub>3</sub> (Pm3m phase) with Sr and Co, respectively to model LSCF system [19]. In terms of CoFe, the same phase (Pm3m) had been used to model the generated CoFe on LSCF by the exsolution. The PBE bulk lattice constants of CoFe (a = b = c = 2.84  $\mathring{A}$ ) and LSCF (a = b = c = 3.89  $\mathring{A}$ ) are used to fix the lateral dimensions of CoFe and LSCF slabs, respectively. Recent computational studies had proposed that (100) with Fe termination for CoFe is most energetically favorable[20]. For LSCF slab, many of perovskite structures dominantly have (110) facets [21]. Based on these results, we focused our computational studies on the CoFe (100) and LSCF (110) slabs. The simulated slabs consist of 4 layers with fixed two bottom layers, but other layers are allowed to relax until the forces are less than 0.03 eV/Å.

All computational slab models include a vacuum spacing of  $\sim 20$  Å which is sufficient to reduce the periodic interaction in the surface normal direction. In terms of system size, 2  $\times$  2 unit cells with corresponding 2  $\times$  2  $\times$  1 Monkhorst-Pack k-point meshes are employed.

In the present study, we obtained the free energy, G, of adsorbed species with Eq. 1 where A\*denotes an adsorbed molecule A on a surface. We used DFT to evaluate the energy (E<sub>DFT</sub>) and vibrational frequencies of the adsorbed molecules. The frequencies are used along with statistical partition functions to calculate the zero point energy (ZPE), and vibrational contributions to entropy ( $S_{vib}$ ) and internal energy ( $U_{vib}$ ).

$$G(A^*) = E_{DFT} + ZPE + U_{vib} - TS_{vib}$$

$$\tag{4}$$

A similar expression but one that incorporates RT, rotational and translational degrees of freedom can be used to obtain the free energy of molecular species under ideal gas conditions (G(A(g))). We evaluated the potential dependent reaction free energy ( $\Delta G$ ) for a coupled proton-electron elementary reaction by using the computational hydrogen

electrode (CHE) model [22]. The  $\Delta G$  of  $A^* + H^+ + e^- \rightarrow AH^*$  can be described by

$$\Delta G = G(AH^*) - G(A^*) - \left[\frac{1}{2}G(H_2) - eU\right]$$
 (5)

where \* indicates an adsorbed molecule on the surface. In the CHE method we use the equivalence of free energy of the proton-electron pair and a hydrogen molecule in the standard state at 0 V of the reference hydrogen electrode (RHE) potential.

#### 3. Results and discussion

#### 3.1. Evolution of hetero-phases

In-situ X-ray diffraction (XRD) was used to examine the crystal structure of the synthesized  $\rm La_{0.7}Sr_{0.2}Co_{0.2}Fe_{0.8}O_3$  (LSCF) powders under air and helium at various temperatures as shown in Fig. S1 and S2. LSCF has a distorted orthorhombic crystal structure at room temperature with a 21 nm of crystallite size. XRD analysis under air and helium gave evidence that LSCF is thermochemically stable up to temperatures of 800 °C. The oxygen vacancy per formula unit of LSCF was calculated, and the stoichiometric formula of LSCF was determined to be  $\rm La_{0.7}Sr_{0.2}Co_{0.2}Fe_{0.8}O_{2.918}$  under helium at 1000 °C.

LSCF underwent structural transformation under 5%  $\rm H_2/N_2$  at 850 °C as demonstrated by the XRD spectra in Fig. 1(a). The main XRD peaks of LSCF remained after 3 h of reduction ( $\rm H_2$ -Red-LSCF), while the additional peaks of bimetallic CoFe, La<sub>2</sub>FeO<sub>4</sub>, and La<sub>2</sub>O<sub>3</sub> is observed. It is important to note that LSCF could be reduced during CH<sub>4</sub> activation since the lattice oxygen from LSCF is consumed to produce  $\rm H_2O$  and  $\rm CO_2$ . To verify the structural transformation of LSCF during CH<sub>4</sub> activation, LSCF treated with 10% CH<sub>4</sub>/He for 3 h at 850 °C (CH<sub>4</sub>-Red-LSCF) was examined by XRD. XRD pattern of the CH<sub>4</sub>-Red-LSCF experienced the same structural transformation with  $\rm H_2$ -Red-LSCF, displaying peaks present in the bimetallic CoFe alloy and La<sub>2</sub>FeO<sub>4</sub>. Following are the steps involved during the structural transformation:

$$nABO_3 \rightarrow (n-1)ABO_3 + AO + BO_2 \tag{6}$$

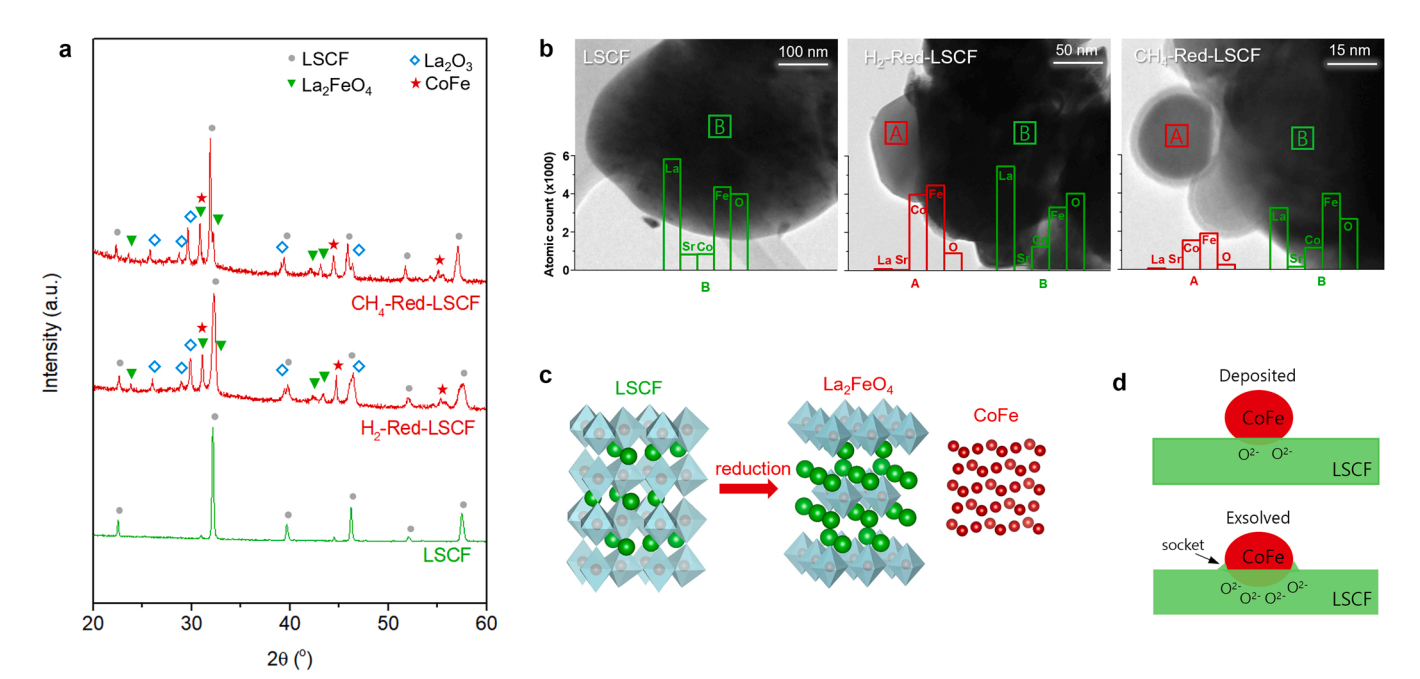


Fig. 1. Evolution of hetero-phases on LSCF under reducing environment. (a) XRD patterns of LSCF,  $H_2$ -Red-LSCF, and  $CH_4$ -Red-LSCF, (b) STEM images of LSCF,  $H_2$ -Red-LSCF, and  $CH_4$ -Red-LSCF with average elemental counts in the specified area shown by a square, (d) illustration of physically deposited CoFe nanoparticle and exsolved CoFe nanoparticles on LSCF.

$$BO_2 + H_2 \rightarrow B + H_2O \quad ABO_3 + AO \rightarrow A_2BO_4$$
 (7)

Consequently, the reduction of LSCF could cause the formation of a B-site zerovalent metal, an  $A_2BO_4$  oxide phase, an A-site metal oxide, and oxygen vacancies as demonstrated in Fig. 1(c), modifying the structural and catalytic properties of the parent perovskite.

Scanning transmission electron microscopy (STEM) equipped with energy dispersive X-ray spectroscopy (EDS) was used to investigate surface morphology of LSCF, H2-Red-LSCF, and CH4-Red-LSCF. In Fig. 1 (b), LSCF showed uniform morphology without any noticeable heterogeneous phase. On the other hand, H2-Red-LSCF clearly exhibited a heterogeneous phase on the surface, indicative of exsolved metal particles. Based on EDS micrographs, atomic counts on the area indicated by a square shape on the STEM images showed that the chemical compositions in the "B" areas are close to LSCF perovskite, while the atomic counts of Co and Fe were found to be substantially higher with approximately equal ratios of Co to Fe in the "A" areas on both H2-Red-LSCF and CH<sub>4</sub>-Red-LSCF. It can be suggested that the nanoparticles are composed of a metallic CoFe alloy, which agrees with the XRD results. The chemical composition of CoFe alloy nanoparticles could vary locally [23]. Nanoparticles exsolved from CH<sub>4</sub>-Red-LSCF appear to have a core-shell appearance, as if they were coated with a thin layer. The shell layer could not be analyzed by EDS, but it can be assumed to be an amorphous carbon phase deposited on the metal surface since graphitic carbon was not detected by XRD. The results temperature-programmed oxidation by CO2 (CO2-TPO) and the sequential temperature-programmed oxidation by O2 (O2-TPO) in Fig. S3 showed that deposited carbon on CH<sub>4</sub>-Red-LSCF was mostly amorphous carbon, which can be readily removed [24]. It was also found that about half of the diameter of each nanoparticle is embedded onto the surface of LSCF so that each nanoparticle is firmly anchored on the LSCF surface, thereby preventing agglomeration while facilitating ionic transfer, as demonstrated in Fig. 1(d). Similar observations have been reported for Ni doped perovskites [25,26].

Based upon the XRD patterns of Red-LSCF, Rietveld refinement method was applied for a quantitative analysis in Fig. 2. Perovskite phase was still the dominant structure in both H2-Red-LSCF (44.1%) and CH<sub>4</sub>-Red-LSCF (51.1%) after the reduction. Each sample exhibited substantial amounts of Ruddlesden-Popper phase, La<sub>2</sub>FeO<sub>4</sub>, that provides a superior level of electrical conductivity over the parent perovskite because of its oxygen hyper stoichiometry [27]. The CoFe alloy was estimated to be present at weight fractions of 11.3% and 8.3% on H<sub>2</sub>-Red-LSCF and CH<sub>4</sub>-Red-LSCF, respectively. The extent of exsolution, ξ, the ratio of moles of CoFe to the moles of the parent perovskite, was calculated to be 0.520 for  $H_2\text{-Red-LSCF}$  and 0.224 for  $CH_4\text{-Red-LSCF}$ [13]. The extent of exsolution can be controlled by various factors such as reduction temperature, duration time, partial pressure of oxygen, and stoichiometry of perovskite. The A-site deficiency of the perovskite in this study could contribute to the significant extent of exsolution since it has been demonstrated that A-site deficient materials display increased migration of B-site cations compared to their stoichiometric equivalents [28].

The transformed structure of LSCF and the exsolved nanoparticles can be revered to the original LSCF structure under oxidizing conditions as verified by XRD and temperature-programmed experiments in Fig. 3. The reduction features obtained by following the  $H_2O$  (m/z=18) signal in the temperature-programmed reduction (TPR) profile in Fig. 3(a) were observed at two different temperatures; one between 400 °C and 600 °C and the other above 700 °C. The first peak is mainly due to the formation of oxygen vacancies, which is the first step of the reduction process and, therefore, can be associated with the partial reduction of Fe<sup>3+</sup> and Co<sup>3+</sup> ions to lower valent cations. At temperatures higher than 700 °C, the reduction of the B-site cations continues, leading to a broad reduction peak. This peak resulted from metal ions being reduced to the metallic phase, causing nanoparticles to be exsolved on the surface. Temperature-programmed oxidation (TPO) was conducted on  $H_2$ -Red-

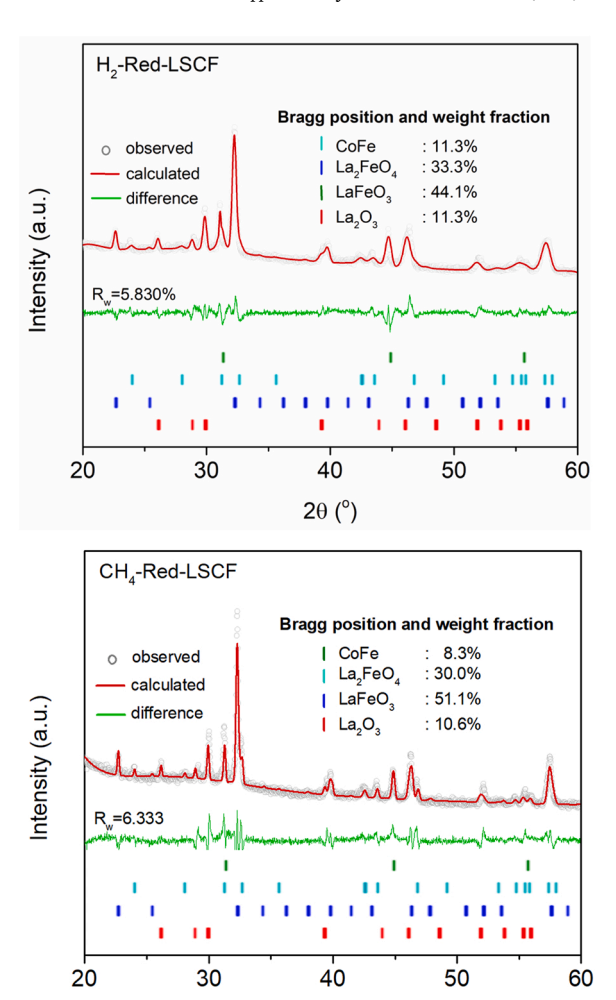


Fig. 2. Rietveld refinement analysis on H<sub>2</sub>-Red-LSCF and CH<sub>4</sub>-Red-LSCF.

2θ (°)

LSCF to estimate the temperature at which reoxidation occurs. The oxygen consumption peak (m/z=32) was observed at 610 °C in the TPO profile. In addition, the XRD pattern of H<sub>2</sub>-Red-LSCF in Fig. 3(b) was completely reversible to the original perovskite structure with no impurity after 1 h of oxidation under 5% O<sub>2</sub>/He atmosphere at 850 °C. Accordingly, the exsolved CoFe nanoparticles on the surface could be readily redistributed when needed.

### 3.2. Electrocatalytic oxidative coupling of methane

The electrocatalytic performance of LSCF was investigated for oxidative methane coupling (OCM) with 10 sccm of CH<sub>4</sub> flow. The product selectivity of OCM was observed for a period of 3 h under 100 mA cm $^{-2}$  at 850 °C in Fig. S4. A 32.5% increase in the selectivity of C<sub>2+</sub> hydrocarbons, including C<sub>2</sub>H<sub>4</sub>, C<sub>2</sub>H<sub>6</sub>, and C<sub>3</sub>H<sub>6</sub>, was observed from 19.9% to 52.4% over the first 3 h, whereas the selectivity for carbon oxides decreased from 80.1% to 47.6%. *In-situ* reduction of LSCF by CH<sub>4</sub> is likely to be responsible for changes in the selectivity, since LSCF was demonstrated to be reduced at 850 °C under CH<sub>4</sub>.

The electrocatalytic OCM reaction on the *in-situ* reduced LSCF anode produced more  $C_{2+}$  hydrocarbons as the current density increased (Fig. 4(a) and Table 1). It was estimated that the carbon balance of the product stream was close to 100% with no more than 2% error. In comparison with open circuit voltage (OCV), the production rate of  $C_{2+}$  hydrocarbons increased 14 times at 150 mA cm<sup>-2</sup>, verifying that the catalytic formation of  $C_{2+}$  hydrocarbons is an electrocatalytically activated process and that oxidative coupling of  $C_{2+}$  is predominant over

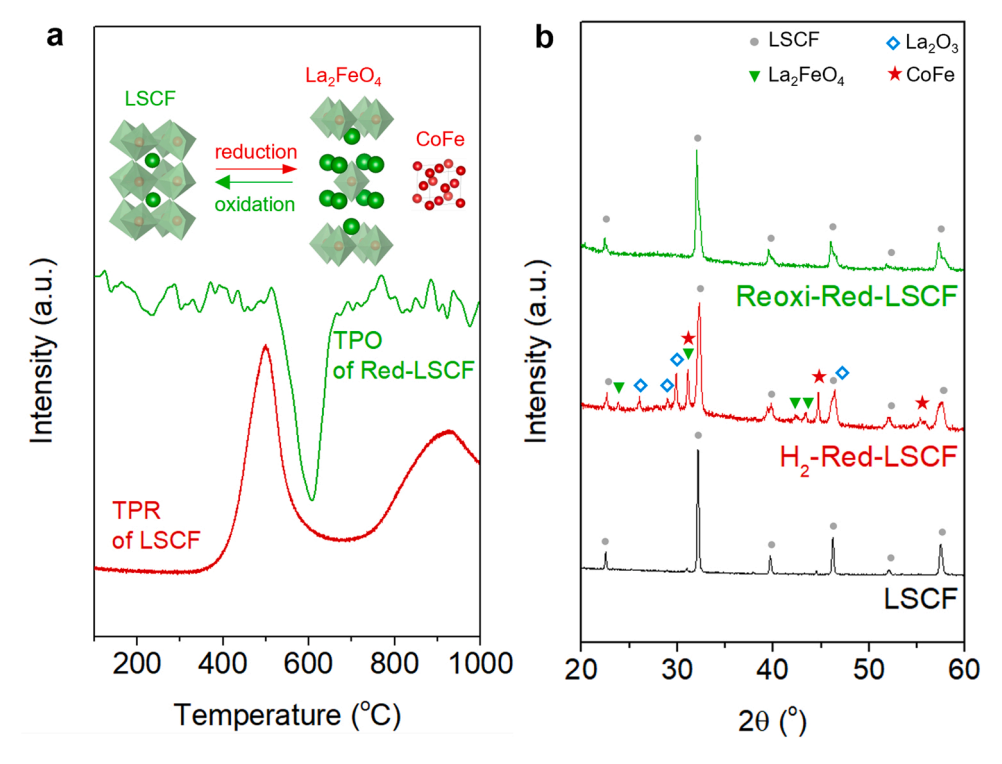


Fig. 3. (a) TPR profiles of LSCF under 5% H<sub>2</sub>/N<sub>2</sub> and TPO profiles of Red-LSCF under 2% O<sub>2</sub>/He, (b) XRD patterns of LSCF, H<sub>2</sub>-Red-LSCF, and re-oxidized Red-LSCF treated with 5% O<sub>2</sub>/He for 1 h at 850 °C (Reoxi-Red-LSCF).

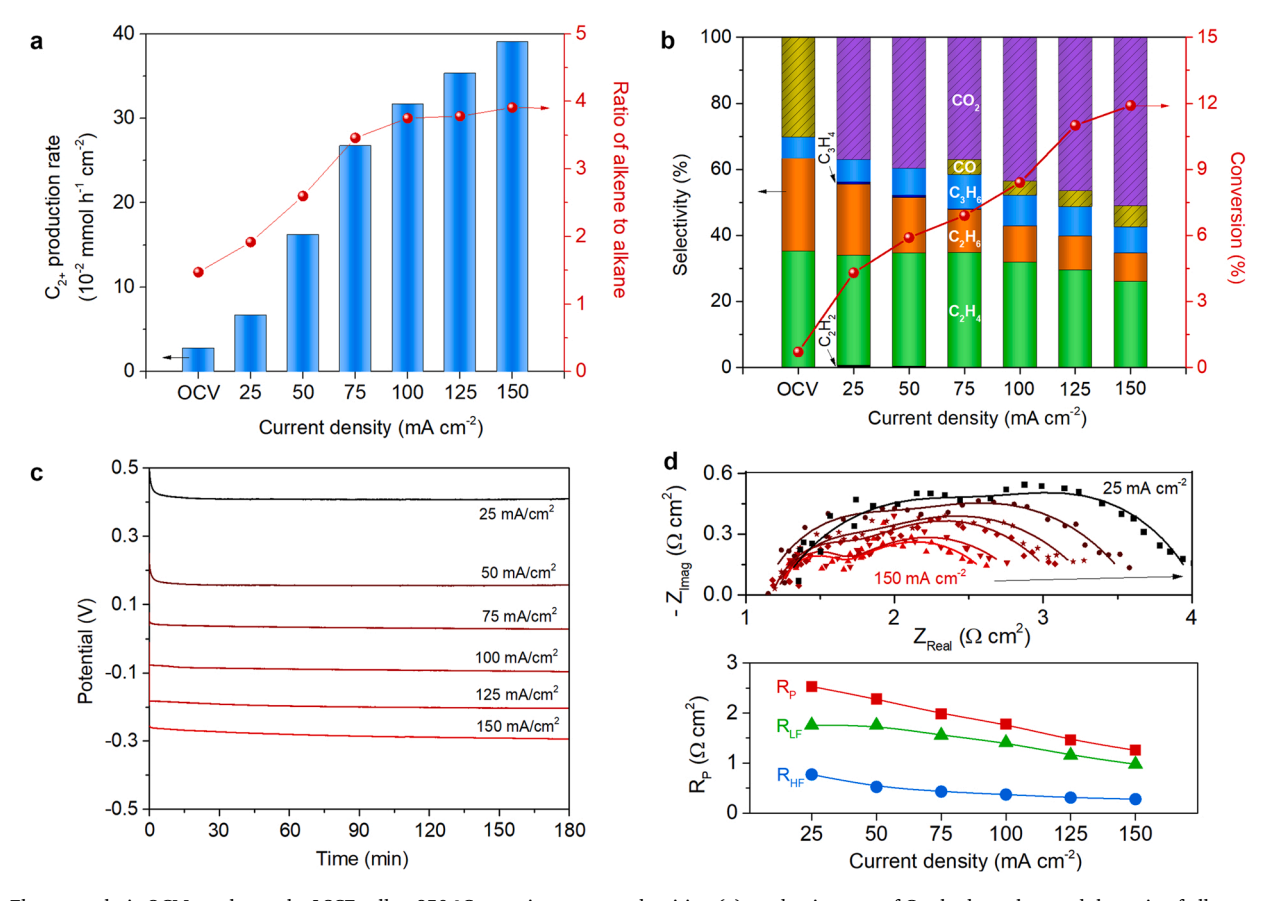


Fig. 4. Electrocatalytic OCM results on the LSCF cell at 850  $^{\circ}$ C at various current densities. (a) production rate of  $C_{2+}$  hydrocarbon and the ratio of alkene to alkane, (b) carbon selectivities and methane conversion, (c) time-on stream of the cell potential, (d) Nyquist plot and polarization resistance.

Table 1 Electrocatalytic OCM results on the LSCF anode at 850  $^{\circ}$ C.

| Current<br>density<br>(mA<br>cm <sup>-2</sup> ) | Carbon Selectivity (%)        |                               |                               |                               |                               |       |                 | C <sub>2+</sub> Selectivity | Production rate of $C_{2+}$ (10 <sup>-2</sup> mmol $h^{-1}$ | Faradaic efficiency (%) (error |
|---|-------------------------------|-------------------------------|-------------------------------|-------------------------------|-------------------------------|-------|-----------------|-----------------------------|---|--------------------------------|
|   | C <sub>2</sub> H <sub>2</sub> | C <sub>2</sub> H <sub>4</sub> | C <sub>2</sub> H <sub>6</sub> | C <sub>3</sub> H <sub>4</sub> | C <sub>3</sub> H <sub>6</sub> | CO    | CO <sub>2</sub> | (%)                         | cm <sup>-2</sup> )  | %)                             |
| OCV   | 0.00                          | 35.25                         | 28.21                         | 0.00                          | 6.28                          | 30.26 | 0.00            | 69.74                       | 2.8   | -                              |
| 25  | 0.65                          | 33.27                         | 21.57                         | 0.89                          | 6.57                          | 0.00  | 37.05           | 62.95                       | 6.7   | 99.5 (3.2)                     |
| 50  | 0.39                          | 34.27                         | 16.74                         | 0.84                          | 8.01                          | 0.00  | 39.75           | 60.25                       | 16.2  | 92.3 (4.3)                     |
| 75  | 0.04                          | 34.77                         | 13.10                         | 0.28                          | 10.23                         | 4.54  | 37.03           | 58.43                       | 26.8  | 88.3 (4.6)                     |
| 100   | 0.05                          | 31.81                         | 10.97                         | 0.24                          | 9.05                          | 4.29  | 43.60           | 52.11                       | 31.7  | 94.9 (3.1)                     |
| 125   | 0.05                          | 29.54                         | 10.19                         | 0.22                          | 8.72                          | 4.77  | 46.51           | 48.72                       | 35.3  | 92.6 (5.3)                     |
| 150   | 0.06                          | 25.94                         | 8.65                          | 0.19                          | 7.64                          | 6.47  | 51.05           | 42.24                       | 39.1  | 94.5 (4.3)                     |

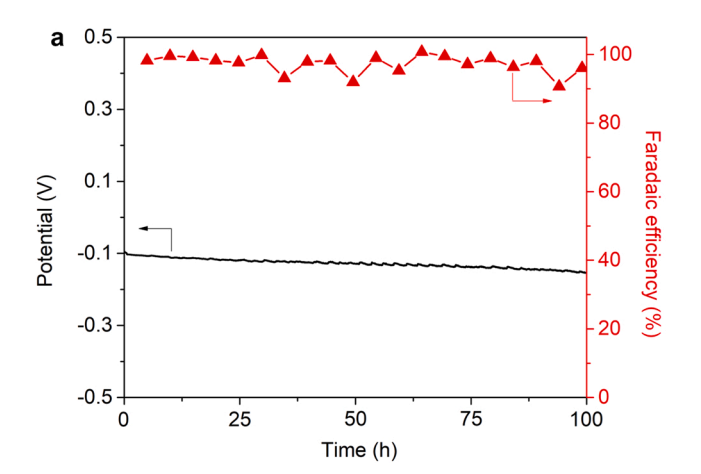
non-oxidative coupling. The increase in the ratio of alkene to alkane implies that the oxidative dehydrogenation of  $C_2H_6$  is also electrocatalytically facilitated, resulting in  $C_2H_4$  being produced about 4 times more than  $C_2H_6$ . It is noteworthy that selectivity to  $C_3H_6$ , which is the most valuable product from OCM, was at 10.23% at 75 mA cm<sup>-2</sup>. Previous studies in the literature have reported propylene selectivities to be less than 2% or negligible [29,30]. This is a significant improvement over existing technology as the large difference in kinetic diameters between  $C_3H_6$  (0.47 nm) and  $CH_4$  (0.38 nm) allow for an easy gas separation, whereas  $C_2H_6$  (0.39 nm) and  $C_2H_4$  (0.39 nm) require a more energy-intensive separation process.

Furthermore, the questioned whether the formation of  $C_2H_4$  is a result of dehydrogenation of  $C_2H_6$  or coupling of  $CH_2$  is also considered to help in the understanding of the reaction pathway. It was found in Fig. S5 that the ratio of  $C_2H_2$  to  $C_2H_4$  increased as the current density increased, while the ratio of  $C_2H_6$  to  $C_2H_4$  decreased. These results suggest that the dehydrogenation of  $C_2H_6$  is the primary step for  $C_2H_4$  production.

The in-situ reduced LSCF cell voltages for OCM remained stable for 180 min (Fig. 4(c)). The stability of the cell at varying current densities can be attributed to the thermochemical stability of the anode after insitu reduction of LSCF under the operating conditions for OCM. Moreover, the cell voltage at 25 mA cm<sup>-2</sup> was 0.41 V indicating that the cell is in a fuel cell regime, capable of producing electricity during OCM catalysis. The in-situ LSCF cell also proved to be efficient for the electrocatalytic OCM, showing over 90% of Faradaic efficiency in Table 1. Raman spectrum on the post-OCM in-situ reduced LSCF anode in Fig. S6 shows small peaks representative of amorphous carbon with no observable peak corresponding to stable graphitic carbon. These results demonstrate that the efficiency loss associated with the formation of carbon on the surface of the in-situ reduced LSCF anode is minimal. The ohmic resistance, R<sub>S</sub>, of the cell remained unchanged at around  $1.25~\Omega~cm^2$  at various current densities (Fig. 4(d)).  $R_P$ , the polarization resistance, considerably decreased with the increase in the current densities. The polarization resistance at high frequency,  $R_{\text{HF}}$ , mainly attributed to charge transfer, was much higher than the one at low frequency, R<sub>LF</sub>, corresponding to mass transfer.

An investigation of the effect of temperature on electrocatalytic OCM has been conducted in the range of 800–850  $^{\circ}\text{C}$  in Fig. S7. The  $\text{C}_{2+}$  hydrocarbon production rate, the  $\text{C}_{2+}$  hydrocarbon selectivity, the ratio of alkene to alkane, and  $\text{C}_3\text{H}_6$  selectivity were all observed the highest at 850  $^{\circ}\text{C}$  at all applied current densities. It is likely because the cleavage of the strong C–H bond in CH<sub>4</sub> molecule requires higher temperature than the subsequent reactions such as methyl coupling to  $\text{C}_2\text{H}_6$ , further dehydrogenation of  $\text{C}_2\text{H}_6$  to  $\text{C}_2\text{H}_4$ , or oxidation to CO and CO<sub>2</sub>.

Fig. 5 shows the results of a long-term electrocatalytic OCM performed on Red-LSCF anode at a constant current density of 100 mA cm $^{-2}$  and an operating temperature of 850 °C. As shown in Fig. 5(a), the Red-LSCF anode showed stable performance over a 100-hour period, with a passivation rate less than 0.5 mV h $^{-1}$  and a Faradaic efficiency greater than 90%, monitored every five hours. The selectivity and production rate of  $C_{2+}$  hydrocarbons were also maintained without significant



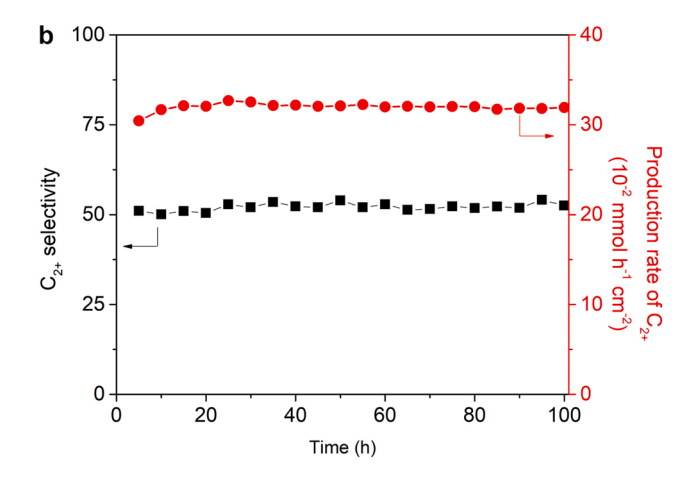


**Fig. 5.** Long-term test of Red-LSCF for the electrocatalytic OCM under 100 mA cm $^{-2}$  at 850 °C. (a) the Red-LSCF cell potential and Faradaic efficiency, (b)  $C_{2+}$  hydrocarbons selectivity and production rate.

change for the period of time in Fig. 5(b). This indicates that the Red-LSCF anode is thermochemically stable under the operating conditions of the electrocatalytic OCM.

#### 3.3. Computational results

The potential-dependent reaction free energy ( $\Delta G$ ) of methane C–C coupling reactions on CoFe and LSCF at 0 V RHE has been studied using DFT. We have explored multiple configurations for each of the intermediates on the surfaces, and Fig. S8 shows the most favored configurations that we have found.

Both surfaces of CoFe (100) and LSCF (110) have coordinatively unsaturated (cus) surface metal sites and cus oxygen atoms. The cus sites of transition metal oxides have been proposed to be generally active due

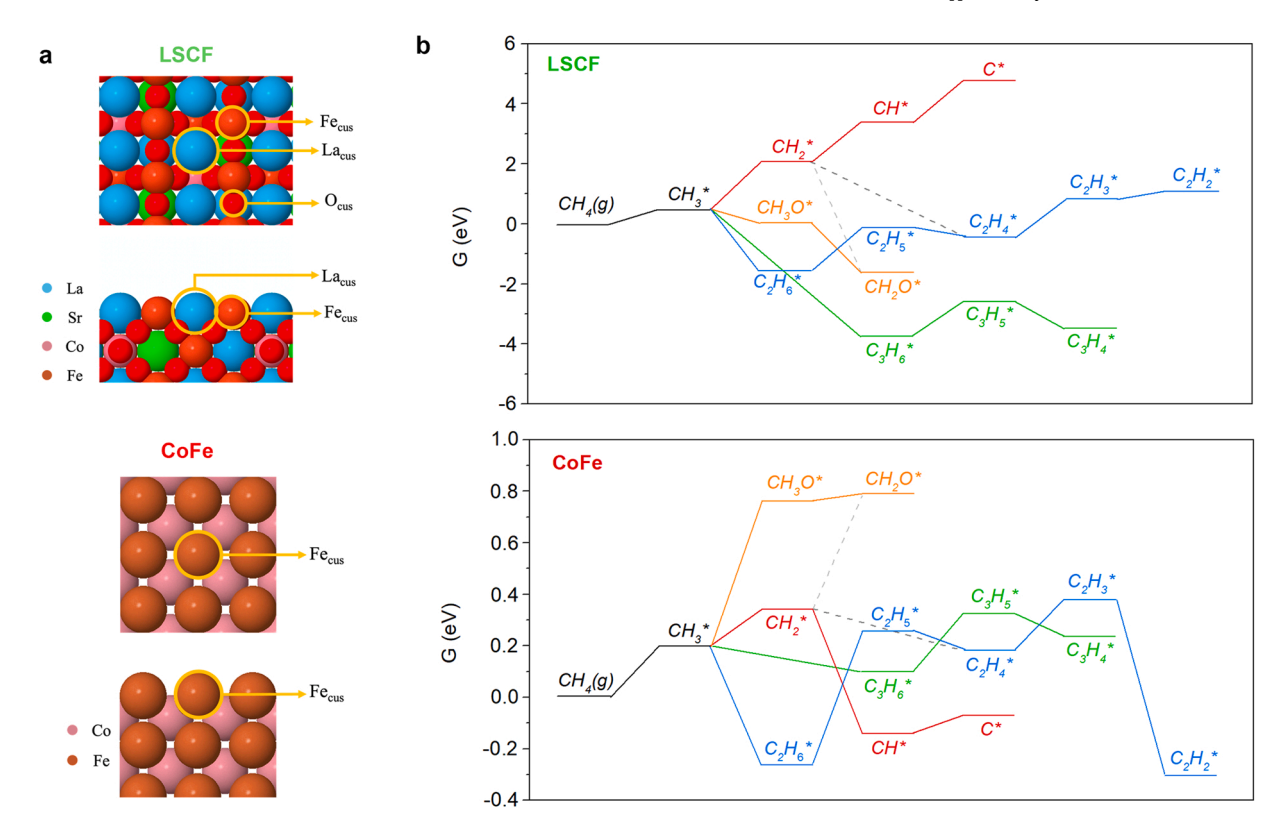


Fig. 6. (a) Surface models of CoFe (100) and LSCF (110). The cus represents coordinatively unsaturated site, and the color schemes are provided in the figures, (b) DFT evaluated free energy diagrams of surface reactions on CoFe and LSCF (110) surface at 0 V RHE.

to the instability of its electronic structures [31]. Fig. 6(a) represents CoFe (100) surface with Fe $_{cus}$  surface atoms and LSCF with La $_{cus}$  and O $_{cus}$ . Co metal atoms of CoFe (100) and LSCF (110) surface are not exposed to the surface.

Fig. 6(b) displays the free energy diagrams of surface reaction on CoFe (100) and LSCF (110) surface calculated by DFT. The v-axis scale is greater on LSCF than CoFe. The initial activation of C-H bond cleavage requires 0.25 eV less energy on the CoFe surface than on LSCF. To form value-added products that were experimentally observed, the generated CH<sub>3</sub>\* on CoFe could undergo two different pathways of C-C coupling: C<sub>2</sub>H<sub>6</sub>\* formation or dehydrogenation to CH<sub>2</sub>\*. The proposed C<sub>2</sub>H<sub>6</sub>\* formation is a non-electrocatalytic step due to the absence of proton-electron transfer. It could continue to occur in gas-phase [7]. C<sub>2</sub>H<sub>6</sub>\* weakly binds on the surface with the low adsorption energy of 0.54 eV; C<sub>2</sub>H<sub>6</sub>\* stability is competitive with the free energy requirement of subsequent dehydrogenation of C<sub>2</sub>H<sub>5</sub> formation (0.56 eV). Considering the activation energy of dehydrogenation and the large entropic contributions of desorption, the C2H6 desorption is expected to occur more frequently than the subsequent dehydrogenation step. The proposed free energy analysis is well in line with the experimental results showing high selectivity of  $C_2H_6(g)$  [32].

 $C_2H_4^{\ast}$  formations can be achieved by the dehydrogenation of  $C_2H_5^{\ast}$  or the non-electrocatalytic C–C coupling of CH<sub>2</sub>\* on CoFe. Both steps are thermodynamically favorable, suggesting that  $C_2H_4^{\ast}$  would be easily formed on CoFe surface.  $C_2H_4$  desorption is thermodynamically less favorable (1.19 eV) than the dehydrogenation (0.21 eV). However, the large entropic contributions of desorption (large desorption prefactor) as well as the kinetic effects of dehydrogenation would allow  $C_2H_4$  desorption to competitive with further dehydrogenation (but still less facile than dehydrogenation). The generated  $C_2H_2^{\ast}$  from the thermodynamically favorable step of  $C_2H_3^{\ast}$  dehydrogenation is stably adsorbed with the large desorption energy of 3.41 eV and likely to undergo oxidation or further dehydrogenation steps. The above computational results of  $C_2H_4^{\ast}$  and  $C_2H_2^{\ast}$  corresponds well to the

experimentally observed higher selectivity of  $\mbox{\rm C}_2\mbox{\rm H}_4$  and low selectivity of  $\mbox{\rm C}_2\mbox{\rm H}_2.$ 

Other pathways for the formation of carbon and longer chain hydrocarbons  $(C_3H_x)$  were also explored. The simulations predicted that the carbon formation by subsequent dehydrogenation from  $CH_3$  are facile: the  $CH_3\to CH_2$  (0.15 eV),  $CH_2\to CH$  (exothermicity), and  $CH\to C$  (0.07 eV). It suggests that carbon coking would competitively occur together with other surface reactions, and it was experimentally observed on CoFe particles as an amorphous layer in Fig. 1(b) and Fig. S6. The C–C coupling forming  $C_3H_6$  is thermodynamically favorable, and the generated  $C_3H_6$  can either desorb (1.3 eV) or undergo subsequent dehydrogenations (0.21 eV).  $C_3H_6$  desorption is expected to compete with the further reaction when considering the large entropic contribution of desorption. Overall, the computational results related to the formations of  $C_3H_6$ ,  $C_2H_6$ , and  $C_2H_4$  showed the low free energy requirements on CoFe surface corresponding to the low applied potentials activating the reactions.

The oxidation pathway starting with  $CH_3^*$  ( $CH_3^* \rightarrow CH_3O^* \rightarrow CH_2O^*$ ) assumes that the oxygen source is LSCF, based on the experimental results. The  $CH_3O^*$  formation (0.61 eV) and the subsequent dehydrogenation (0.03 eV) were predicted to be exothermic reactions resulting in a slower oxidation rate compared to the C–C coupling reactions discussed above. Even though the other oxidation steps could require less energy, the oxidation rate would still be slow due to the lack of surface oxygens on CoFe. The results of DFT calculations suggest that the C–C coupling reaction dominates the reaction pathway, thereby producing high selectivity of  $C_{2+}$  hydrocarbons.

On LSCF surface, C–C coupling and the oxidation steps from CH $_3$ \* are all thermodynamically favorable, except for CH $_3$ \* dehydrogenation. The subsequent dehydrogenation step of C $_2$ H $_6$ \*  $\rightarrow$  C $_2$ H $_5$ \* formation has a large thermodynamic uphill (1.45 eV). In addition, the small desorption energy of C $_2$ H $_6$  (0.22 eV) causes C $_2$ H $_6$  desorption to be favored rather than dehydrogenation. These thermodynamic hindrances of C $_2$ H $_5$ \* and CH $_2$ \* formations and the favorable

 $\rm C_2H_6$  desorption consequently hamper the formation of  $\rm C_2H_4$ . Interestingly,  $\rm C_3H_6$  formation from C–C coupling of CH<sub>3</sub>\* was predicted to be readily achieved due to the thermodynamic favorability on LSCF. The desorption of  $\rm C_3H_6$  is strongly favored over further dehydrogenation because of the low adsorption stability (0.11 eV (desorption) vs. 1.16 eV (dehydrogenation). Overall, the LSCF is expected to favorably produce  $\rm C_2H_6(g)$  and  $\rm C_3H_6(g)$ ; however, these pathways are competitive with the oxidation reactions which corresponds to the low selectivity toward  $\rm C_{2+}$ . By comparing the computational results of CoFe and LSCF, we find that CoFe and LSCF are both attributed to generation of  $\rm C_2H_6(g)$  and  $\rm C_3H_6(g)$ ; however, the generation of  $\rm C_2H_4(g)$  primarily occurs on CoFe while oxidation is dominant on LSCF.

#### 3.4. Analysis of electronic structure

The electronic structure of LSCF and Red-LSCF was investigated to reveal the mechanism for improved performance of Red-LSCF for OCM. X-ray photoelectron spectroscopy (Fig. 7) and X-ray absorption spectroscopy (Fig. 8) techniques were used to characterize these samples.

There were two main peaks in the XPS spectrum of La 3d on LSCF: La  $3d_{3/2}$  and La  $3d_{5/2},$  which were located at  $833.23\;\text{eV}$  and  $850.03\;\text{eV},$ respectively, due to a 16.8 eV spin-orbital splitting, which suggests that La<sup>3+</sup> dominates the spectrum [33]. Furthermore, satellite peaks at 837.3 eV and 854.1 eV are also evidence for the trivalent oxidation state of La ions, which are 3.7 eV higher than the peaks along the 3d<sub>5/2</sub> and 3d<sub>3/2</sub> core lines [34]. Observations of all the above spectral characteristics indicate that lanthanum in LSCF is in an oxidation state of 3 + coordinated by an oxide ion environment. After the reduction of LSCF, the La  $3d_{3/2}$  peak was shifted by 1.13-834.36 eV. This can be explained by the fact that both lanthanum oxide and carbonate contribute to the La 3d spectrum of Red-LSCF. Lanthanum atoms form lanthanum oxide, La<sub>2</sub>O<sub>3</sub>, during the reduction process of LSCF as explained by the results of XRD in Fig. 1. La<sub>2</sub>O<sub>3</sub> having a strong basicity is typically converted to lanthanum carbonate, La<sub>2</sub>O<sub>2</sub>CO<sub>3</sub>, by CO<sub>2</sub> adsorption on its surface under air [35]. Since La<sub>2</sub>O<sub>3</sub>-based catalysts are known for high C2 hydrocarbon selectivity for OCM, the evolution of La<sub>2</sub>O<sub>3</sub> after the reduction of LSCF would contribute to the improved selectivity toward C<sub>2+</sub> hydrocarbons for OCM [35].

Co 2p XPS spectrum on LSCF was deconvoluted into two different oxidation states. Those peaks in the region of Co  $2p_{3/2}$  were observed at 779.8 eV for  $\text{Co}^{3+}$  and 781.5 eV for  $\text{Co}^{2+}$ , respectively [36]. The XPS spectrum of Co 2p on Red-LSCF, each peak in the region of Co  $2p_{3/2}$  was

located at 780.0 eV for  $\mathrm{Co^{3+}}$  and 782.8 eV for  $\mathrm{Co^{2+}}$ , respectively. These shifts in binding energy between LSCF and Red-LSCF were due to the oxygen vacancy formed during the reduction under  $\mathrm{H_2}$ . Moreover, a peak corresponding to zerovalent Co species was observed at 777.8 eV in the regions of Co  $\mathrm{2p_{3/2}}$ . In accordance with the results of TEM and XRD, this peak is evidence of bimetallic CoFe nanoparticles that have been exsolved on the surface during the reduction step.

Analysis of the binding energies between the Fe  $2p_{3/2}$  peak and the Fe<sup>2+</sup> and Fe<sup>3+</sup> satellite peaks has recently been reported as a method for determining the presence of Fe<sup>2+</sup> and Fe<sup>3+</sup> [37].

$$\Delta F e_{2p_{3/2}} = BE \left[ Sat \left( F e_{2p_{3/2}} \right) \right] - BE \left[ F e_{2p_{3/2}} \right]$$
(8)

Fe<sup>3+</sup> compounds normally have about 8 eV of  $\Delta Fe_{2p_{3/2}}$ , while Fe<sup>2+</sup> compounds have 4.3–5.65 eV. In the XPS spectra,  $\Delta Fe_{2p_{3/2}}$  is 8.53 eV for Fe<sup>+3</sup> 2p<sub>3/2</sub> satellite, indicating Fe ions existed as Fe<sup>3+</sup> mixture. The peaks at the binding energy of 709.4 eV and 711.1 eV were assigned to Fe<sup>3+</sup> 2p<sub>3/2</sub> and Fe<sup>4+</sup> 2p<sub>3/2</sub>, respectively, for LSCF [38]. The Fe ions have different oxidation states which provide redox couples, enabling the LSCF to function as a p-type charge carrier [39]. After the reduction of LSCF, the XPS spectra in the region of Fe 2p<sub>3/2</sub> has three deconvoluted peaks. The peaks for Fe<sup>3+</sup> 2p<sub>3/2</sub> and Fe<sup>4+</sup> 2p<sub>3/2</sub> were shifted to the binding energy of 710.1 eV, and 711.8 eV, respectively. The composition of Fe ions with higher oxidation state decreased from 64.7% to 53.2% for Fe<sup>4+</sup>. Moreover, it displayed the peak at 706.3 eV associated with the zerovalent iron from the exsolved bimetallic CoFe nanoparticles. Such zerovalent bimetallic CoFe nanoparticles would provide highly selective conversion of CH<sub>4</sub> toward C<sub>2+</sub> hydrocarbons.

The XPS spectra of Sr 3d in LSCF and Red-LSCF was composed of a pair of species with an oxidation state of 2+. Sr existed in three divalent oxide forms with different  $3d_{5/2}$  binding energies at 131.8, 132.8, and 133.6 eV. The first value is close to that reported for La<sub>0.6</sub>Sr<sub>0.4</sub>Co<sub>0.8</sub>Fe<sub>0.2</sub>O<sub>3-\delta</sub>, and the other two peaks may reflect strontium oxide (SrO) and strontium carbonate (SrCO<sub>3</sub>) [10,40]. The reduction of LSCF resulted in an increased concentration of oxygen vacancies on the surface facilitating an adsorption of CO<sub>2</sub>, and strontium atoms easily react with CO<sub>2</sub> to form stable SrCO<sub>3</sub>. SrO with strong basicity formed on LSCF could have contributed to the improvement in selectivity of C<sub>2+</sub> hydrocarbons as SrO is likely to segregate on the surface [35].

Fig. 8 illustrates XANES spectral analysis of the Co K-edge and Fe K-edge for LSCF and Red-LSCF with reference metal foils and oxides. Observations of Fe K-edge XANES spectra in Fig. 8(a) show a shift downward of -1.3 eV from 7127.6 eV to 7126.3 eV after the reduction.

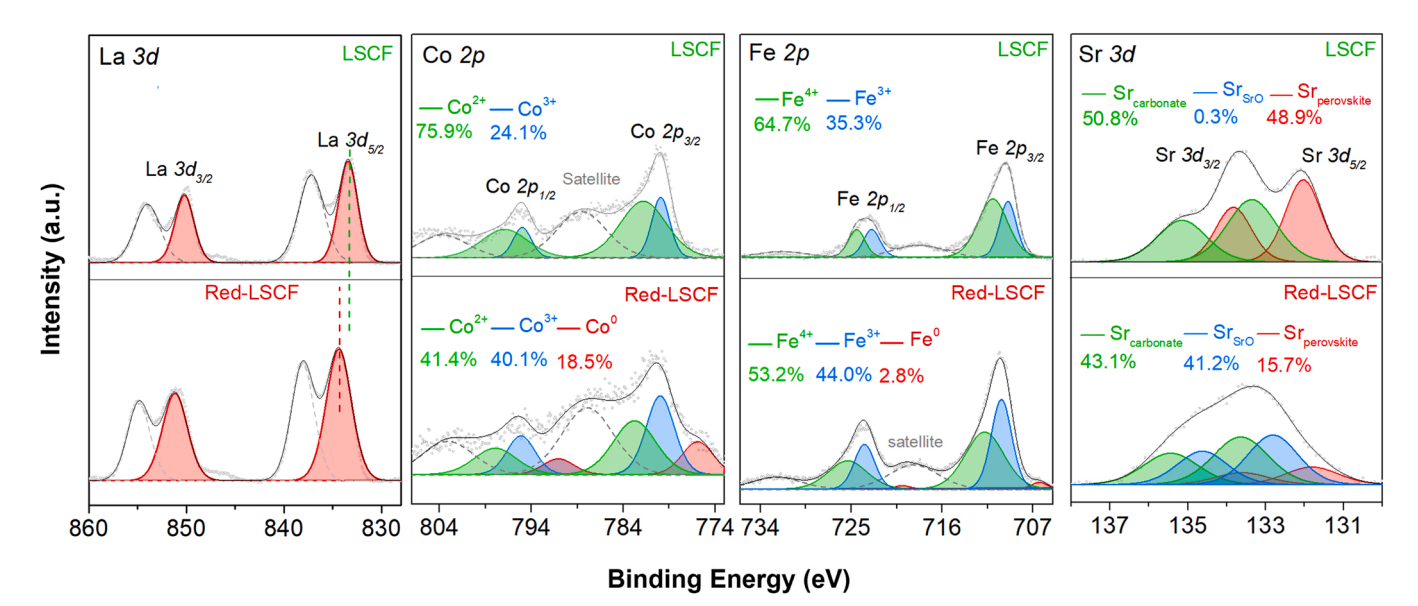


Fig. 7. X-ray photoelectron spectra of LSCF and Red-LSCF.

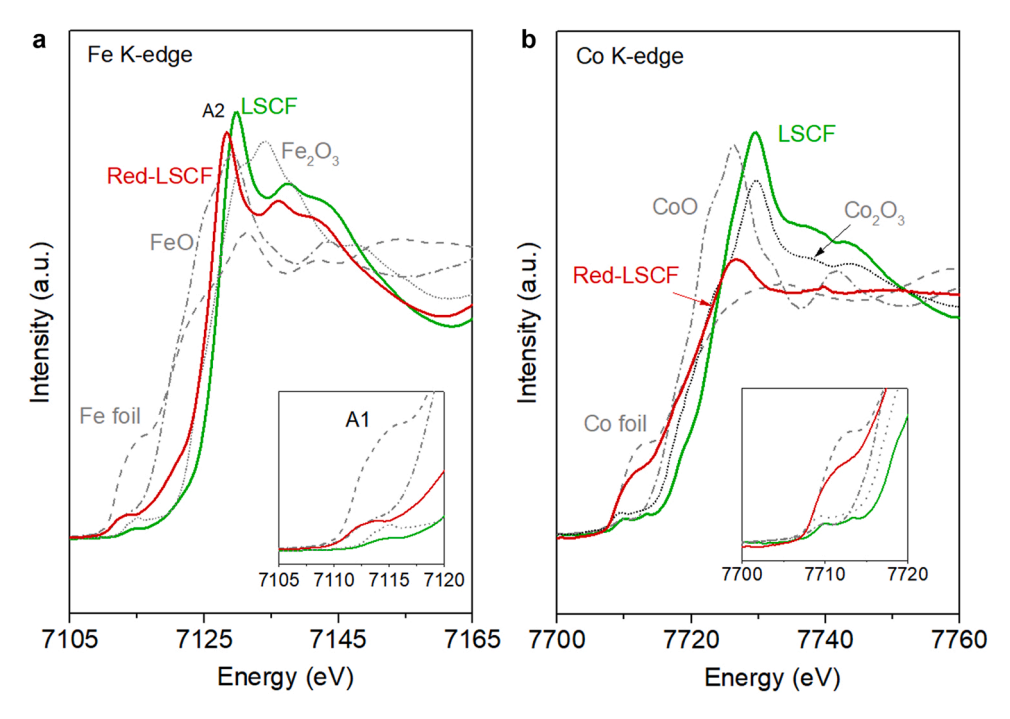


Fig. 8. XANES spectra on LSCF and Red-LSCF.

As the absorption edge energy of the reference compound Fe $_2O_3$  is 7126.14 eV, it is obvious that Red-LSCF and LSCF exhibit a predominantly 3+ oxidation state. Additionally, two peak features are observed on both samples, namely pre-edge peak  $A_1$  and post-edge peak  $A_2$  [41].

In response to the reduction of LSCF, the A1 peak shifted slightly from 7114.3 eV to 7112.9 eV and its intensity increased. The decrease in the edge  $A_2$  was observed indicative of the reduced oxidation state of Fe ions in Red-LSCF.

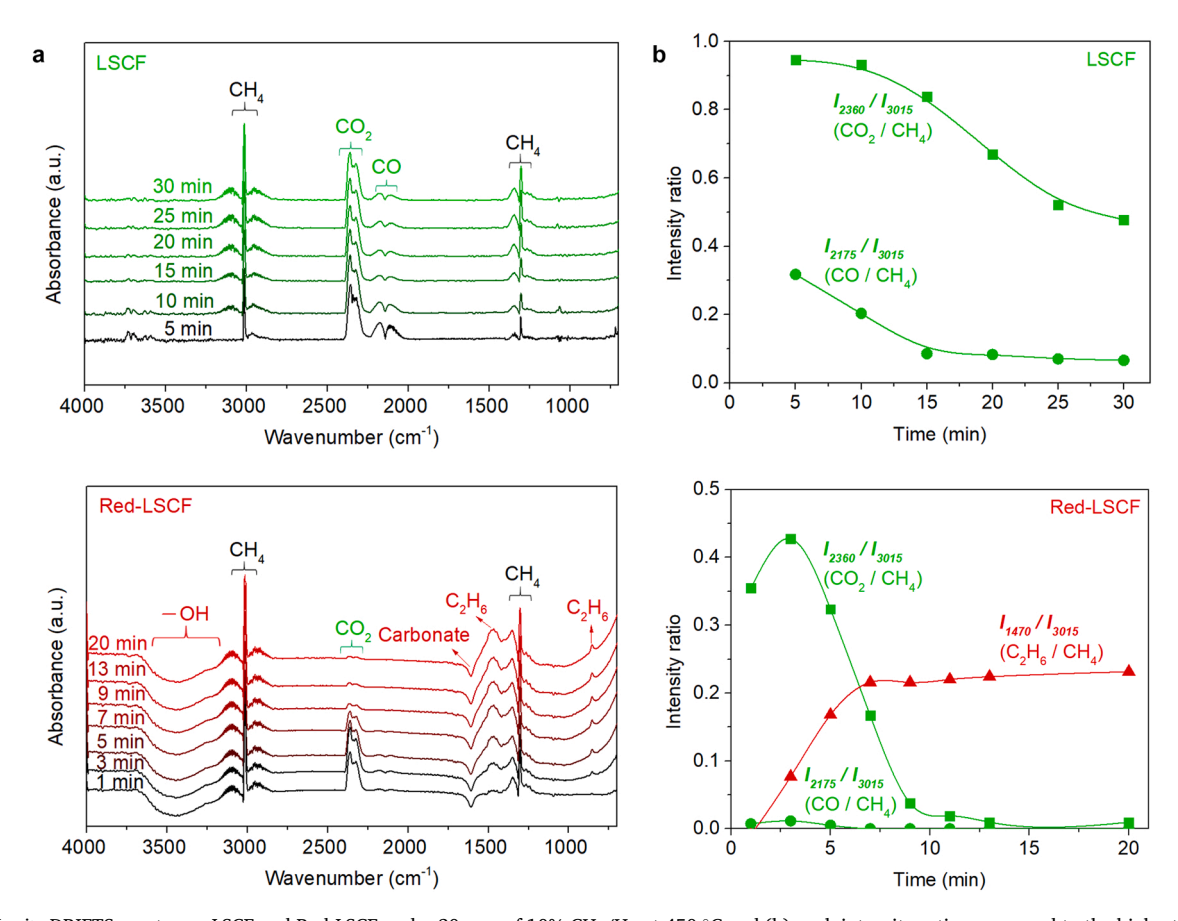


Fig. 9. (a) In-situ DRIFTS spectra on LSCF and Red-LSCF under 30 ccm of 10% CH<sub>4</sub>/He at 450 °C and (b) peak intensity ratios compared to the highest peak of CH<sub>4</sub> at 3015 cm<sup>-1</sup>.

The Co K-edge energy decreased to 7717.7 eV from 7723.6 eV attributed to the reduction treatment in Fig. 8(b). The inset in Fig. 8(b) shows the split of the pre-edge peak of Co K-edge on LSCF, but not on Red-LSCF, meaning that cobalt predominantly exists in the zerovalent form on Red-LSCF. Co pre-edge peak on Red-LSCF exhibits a high intensity near the Co foil, and the one on LSCF shows a low intensity comparable to  $\text{Co}_2\text{O}_3$ . In addition, we found that there was a significant reduction in the white line intensity in the Co K-edge XANES spectrum following the reduction of LSCF. The reason for this is that Red-LSCF containing the metallic species has less well-defined energy levels than LSCF, resulting in lower intensity of the white line closer to Co foil. The ligand-to-metal charge transfer (LMCT) also undergoes a mixed configuration in the ground and excited states following the reduction of LSCF, which leads to a dispersion of the white line [42].

The average oxidation state of cobalt and iron ions in the samples were estimated based on the linearly fitted oxidation state as a function of energy in Fig. S9. The reduction of the samples resulted in the oxidation state of iron decreasing from 3.03 to 2.81 and cobalt from 2.27 to 1.28.

#### 3.5. In-situ DRIFTS and TPSR under CH4

In order to gain insight into the surface dynamics during CH<sub>4</sub> activation, in-situ CH<sub>4</sub>-DRIFTS experiments were performed on LSCF and Red-LSCF catalysts under CH<sub>4</sub> atmosphere at 450 °C. As shown in Fig. 9, in-situ CH4-DRIFTS spectra on LSCF showed two pairs of adsorption peaks in addition to the peaks of gaseous CH<sub>4</sub>. The peaks characterized by the IR bands in the region of 2360 cm<sup>-1</sup> and 2325 cm<sup>-1</sup> are corresponding to molecularly adsorbed CO<sub>2</sub> [43]. The peaks located at 2175 cm<sup>-1</sup> and 2110 cm<sup>-1</sup> are attributed to molecularly adsorbed CO [44]. Those peaks originated from the oxidation of CH<sub>4</sub> on the surface of LSCF. The intensity of those peaks decreased progressively in 20 min. The peak intensity ratio compared to the highest peak of CH<sub>4</sub> at  $3015~\text{cm}^{-1}$  clearly illustrates the peak evolution of the carbon oxides in Fig. 9(b).  $I_{2360}$  /  $I_{3015}$  (CO<sub>2</sub>/CH<sub>4</sub>) was estimated above 0.9 for the first 10 min of the reaction and gradually decreased to 0.5.  $I_{2175}$  /  $I_{3015}$ (CO/CH<sub>4</sub>) behaved similarly. This decrease in peak intensity ratio is likely due to the limited amount of surface oxygen on the LSCF. The in-situ DRIFTS with CH4 on Red-LSCF also displayed the IR bands corresponding to molecularly adsorbed CO2 and CO. The DRIFTS spectra also showed two peaks located at 1470 cm<sup>-1</sup> and 850 cm<sup>-1</sup> which are ascribed to the adsorbed C<sub>2</sub>H<sub>6</sub> [45]. The intensity ratio on Red-LSCF in Fig. 9(b) showed that  $I_{1470} / I_{3015}$  (C<sub>2</sub>H<sub>6</sub>/CH<sub>4</sub>) increased from 0 to 0.23, while  $I_{2360}$  /  $I_{3015}$  (CO<sub>2</sub>/CH<sub>4</sub>) and  $I_{2175}$  /  $I_{3015}$  (CO/CH<sub>4</sub>) decreased to below 0.1 within 10 min. This result implies that the surface oxygen available from Red-LSCF was rapidly consumed, and CH4 coupling took place predominantly when oxygen is limited. Therefore, it could be suggested that CH<sub>4</sub> coupling reactions to C<sub>2+</sub> hydrocarbons are competing with the oxidation of CH<sub>4</sub> and controlling the oxygen supply is a key parameter for a selective conversion of CH<sub>4</sub> on Red-LSCF.

In addition, with the introduction of CH<sub>4</sub>, a broad negative band was found at 3480 cm<sup>-1</sup> in the DRIFTS spectra of Red-LSCF. Since the peak in that region is corresponding to the stretch mode of -OH group, the negative intensity of the peak implies that the hydroxyl groups on the surface of Red-LSCF were consumed during CH4 adsorption and activation [46]. The dissociative adsorption of CH<sub>4</sub> might predominantly occur on the surface of the exsolved bimetallic CoFe nanoparticles at such low operating temperature of 450 °C. Then, in view of the well-known phenomenon of hydrogen spillover, the adsorbed H atoms dissociated from CH<sub>4</sub> on CoFe nanoparticles may react with -OH groups on the surface of LSCF, releasing H<sub>2</sub>O [47]. An additional negative peak near 1610 cm<sup>-1</sup> can be attributed to bidentate carbonate [48]. As demonstrated by the XPS results, carbonate species readily form on the reduced surface of LSCF. With the introduction of CH<sub>4</sub>, the negative peak was immediately observed, indicating that the two bidentate carbonates, consisting of La<sub>2</sub>O<sub>2</sub>CO<sub>3</sub> and SrCO<sub>3</sub>, are consumed rapidly to react

with CH<sub>4</sub>.

An experiment concerning the activation of CH4 by LSCF and Red-LSCF was conducted by monitoring temperature-programmed surface reaction with CH<sub>4</sub> (CH<sub>4</sub>-TPSR). Fig. 10 shows the product molecules arising from the reaction as CH4, H2, and CO from each catalyst. The formation of CO and H2 on LSCF took off sharply at a temperature of 760 °C. As of 867 °C, the CO production was completed, but the H<sub>2</sub> production was still in progress up to 930 °C. It was also observed that small amounts of H<sub>2</sub>O and CO<sub>2</sub> evolved during the reaction, which could be seen in the 50 times enlarged plots. It is interesting that CO2 signal abruptly decreased at 770 °C, suggesting a contribution from the reverse-water gas shift (r-WGS) reaction. We assume that in-situ reduction under CH<sub>4</sub> flow caused the exsolution of CoFe nanoparticles on the surface of LSCF during the heating process, resulting in the reaction mechanism being changed. For Red-LSCF, CH<sub>4</sub> activation toward H<sub>2</sub> and CO took place readily when the temperature was above 672 °C. In light of the much lower temperature for activating CH<sub>4</sub> on Red-LSCF than on LSCF, it is apparent that Red-LSCF is a more effective catalyst for CH<sub>4</sub> activation than LSCF. In addition, TPSR profiles taken on Red-LSCF showed to have a peak intensity of H<sub>2</sub> greater than CO, supporting the validity of the finding that the deep oxidation of CH<sub>4</sub> can be suppressed by the reduction of LSCF. In the enlarged plot, CO2 signal was much lower than CO signal in the entire temperature range, indicating that CH<sub>4</sub> activation on CoFe primarily produces CO rather than CO<sub>2</sub>. It supports again that the abrupt decrease in CO2 signal intensity in TPRS on LSCF is due to the in-situ exsolved CoFe nanoparticles.

The majority of carbon products from TPSR was CO rather than  $CO_2$  and  $C_{2+}$  hydrocarbons on both LSCF and Red-LSCF. Given that CO was produced without  $CO_2$  from OCM under OCV in Fig. 4(b), the surface oxygen on LSCF perovskite can be assumed to be responsible for the production of  $CO_2$ .

#### 3.6. Analysis of surface basicity

It is important to note that heterogeneous phases such as La<sub>2</sub>O<sub>3</sub>, La<sub>2</sub>FeO<sub>4</sub>, and exsolved CoFe nanoparticles formed during the reduction of LSCF could affect its adsorption and desorption properties. According to the statistical analysis of published data from the last three decades on OCM, Zavyalova et al. have discovered several key factors for the OCM catalysts and demonstrated strong basicity as one of the most crucial factors for the selective formation of C<sub>2+</sub> products [49]. It is not surprising that an extremely strong base is required to activate CH<sub>4</sub>, given that CH<sub>4</sub> is an extremely weak acid. TPD-DRIFTS using CO<sub>2</sub> as a probe molecule was conducted on LSCF and Red-LSCF to illustrate the difference in the acidic/basic characteristics of both samples. As shown in Fig. 11, CO<sub>2</sub> was molecularly adsorbed onto both samples as evidenced with the peaks at 2380 cm<sup>-1</sup> and 2330 cm<sup>-1</sup> [43]. When the temperature was raised to 350 °C, it is apparent from both samples that the peak intensities of physisorbed CO2 decreased to zero. On the other hand, chemisorbed forms of carbonate were only observed on the Red-LSCF with the adsorption peaks located at 1530 cm<sup>-1</sup> and 1380 cm<sup>-1</sup>, corresponding to bidendate and monodendate carbonate, respectively [44]. It was observed that adsorbed carbonates could withstand temperatures up to 350  $^{\circ}$ C. The peaks of carbonated species could be originated from the formation of lanthanum carbonate (La<sub>2</sub>O<sub>2</sub>CO<sub>3</sub>) and strontium carbonate (SrCO<sub>3</sub>) in agreement with XPS analysis shown in Fig. 7. According to this, the presence of oxygen vacancies and exsolution of CoFe alloy nanoparticles induced by the reduction of LSCF promotes the basicity of LSCF and facilitates CO2 adsorption. It is a well-established fact that thermodynamically stable carbonate is a substantial constituent in initiating the oxidation of CH<sub>4</sub> on its surface [50]. Therefore, it can be stated that the surface of Red-LSCF is more basic than that of LSCF and the reduction of LSCF is an effective way of promoting the catalytic characteristics of LSCF for OCM.

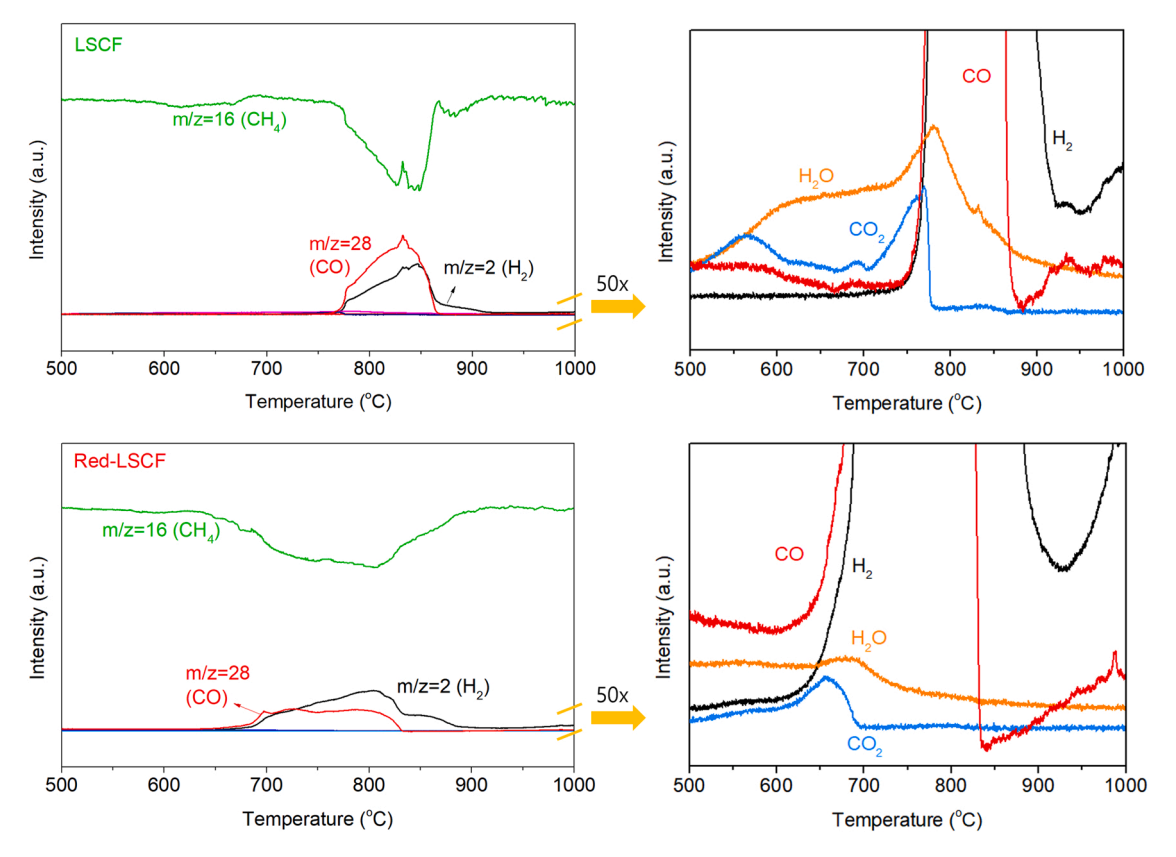


Fig. 10. TPSR profiles on LSCF and Red-LSCF under 30ccm of 10% CH<sub>4</sub>/He.

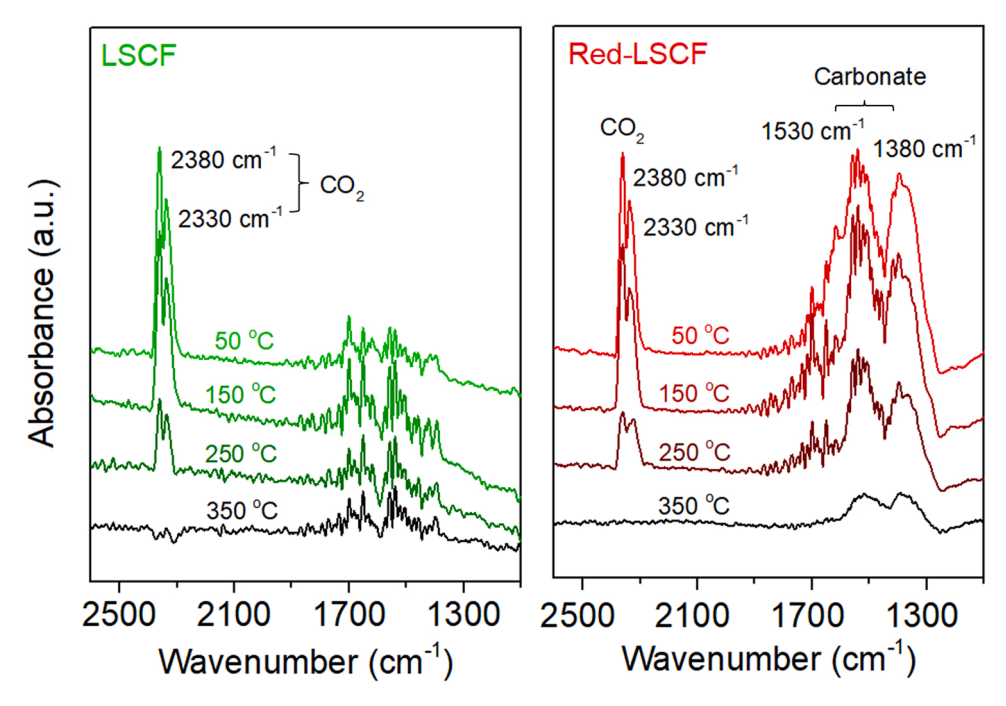
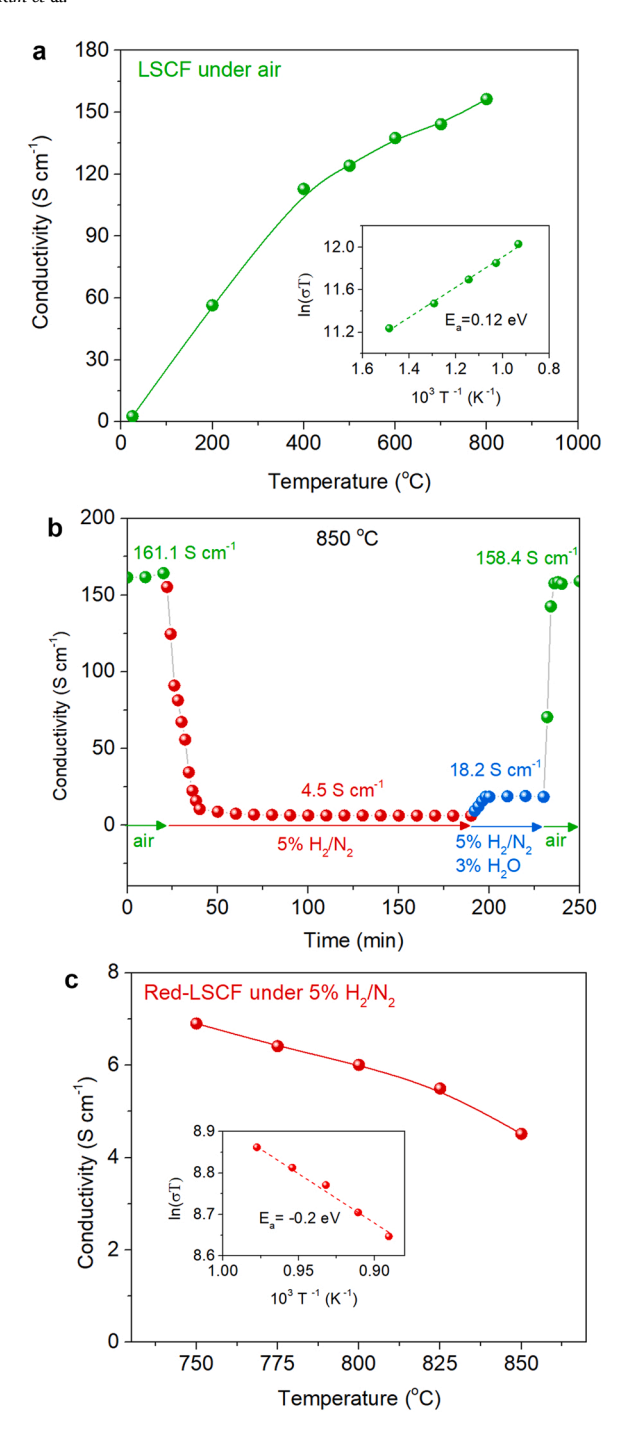


Fig. 11. In-situ TPD-DRIFTS of CO<sub>2</sub> on LSCF and Red-LSCF at various temperatures.

#### 3.7. Electrical conductivity

The electrical conductivity of LSCF and Red-LSCF was measured in air and  $5\%~H_2/N_2$  environment in Fig. 12 to evaluate the conductivity of the LSCF electrodes under the environment similar with the electrocatalytic OCM.

A high electrical conductivity was observed with LSCF at elevated temperature under air in Fig. 12(a). According to the linearly fit Arrhenius plot, LSCFs follow a small polaron conduction mechanism with Fe $^{3+}$ /Fe $^{4+}$  redox couples acting as p-type carriers [11]. The LSCF pellet was highly conductive under air at elevated temperatures with a maximum conductivity of 173 S cm $^{-1}$ , proving to be a reliable electrode.



**Fig. 12.** *In-situ* measurement of electrical conductivity under different atmospheres. (a) LSCF under air as a function of temperature, (b) LSCF under different atmospheres at 850 °C, (c) Red-LSCF under 5%  $\rm H_2/N_2$  as a function of temperature. The inset figures show Arrhenius plots with activation energy.

A substantial decrease in electrical conductivity was observed for LSCF in Fig. 12(b) when exposed to 5%  $\rm H_2/N_2$  at 850 °C, from 173 S cm<sup>-1</sup> to 6.1 S cm<sup>-1</sup>, within 15 min and then gradually decreased more to 4.5 S cm<sup>-1</sup>. Such decrease in electrical conductivity has been observed on ( $\rm La_{0.75}Sr_{0.25})_{0.95}Cr_{0.5}Mn_{0.5}O_3$  under reducing environment, while strontium titanate-based perovskite showed an increased in conductivity after reduction [51,52]. The abrupt decrease in the electrical conductivity could not be explained by the structural transformation of LSCF which occurs much slower. Then, it could be attributed to the formation of oxygen vacancies. Electrical conductivity of lanthanum ferrite based perovskites have shown the decrease in conductivity at

high temperatures since outgoing oxide ions leave oxygen vacancies resulting in the reduced concentration of Fe ions redox pairs [53]. In addition to oxidation state of B-site ions, electric conductivity may vary depending on the Fermi level. According to an *in- situ* AP-XPS study, electron holes tend to be located on O 2p states since oxygen vacancies are much larger than electronic defects at oxygen partial pressures of less than 0.1 mbar [54]. A further observation was made in an *in-situ* XAS study that the anodic polarization resulted in depopulation of electronic states of the Fe<sup>3+</sup>/Fe<sup>4+</sup> redox couples near the Fermi level [55].

After exposure to the reducing atmosphere,  $3\%~H_2O$  with  $5\%~H_2/N_2$  was introduced while measuring the conductivity since  $H_2O$  is a product for OCM reaction affecting the conductivity of the LSCF anode. The electrical conductivity increased up to  $18.2~S~cm^{-1}$  under the humid conditions, which is above the generally acceptable level of conductivity,  $1~S~cm^{-1}$  for porous electrode structures and  $10~S~cm^{-1}$  for densified electrode materials for SOEC/SOFC [56]. Therefore, the reduced LSCF may work properly as an electrocatalysts for the electrocatalytic OCM under a humid reducing environment with sufficient electrical conductivity.

The redox reversibility was also observed in the electrical conductivity in Fig. 12(b). When 10%  $\rm O_2/H_2$  was introduced, the conductivity increased back to the original level in a few minutes.

A noteworthy observation is that the electrical conductivity of Red-LSCF had a negative dependency on temperature in Fig. 12(c). However, it seems to still follow the small polaron conduction mechanism considering the linearly fit Arrhenius plot. Such negative relation of electrical conductivity to temperature has been studied on  $\rm Sr_2Fe-Mo_{0.65}Ni_{0.35}O_6$  [57]. The decrease in the electrical conductivity with the increase in the temperature is likely due to the abundant oxygen vacancies resulted from the reducing atmosphere and high temperatures.

#### 4. Conclusions

The exsolved B-site metal nanoparticles on the perovskite surface has been recognized as an important factor in the improvement of electrocatalytic activity. By reducing LSCF perovskite in-situ, its surface properties were modified and its electrocatalytic activity for OCM was improved by 32.5%. XRD and STEM equipped with EDS experiments proved that the evolution of hetero-phases during LSCF reduction under H<sub>2</sub> or CH<sub>4</sub> resulted in bimetallic CoFe nanoparticles being formed at the surface of LSCF at 850 °C. The structural evolution of LSCF appeared to be completely reversible as reflected in XRD and TPR/TPO patterns. indicating that sintering of nanoparticles on the surface could be addressed by reoxidation and subsequent reduction to re-distribute the exsolved CoFe nanoparticles. As a result of using the LSCF anode either in ion pump mode or in fuel cell mode, the highest C<sub>2+</sub> hydrocarbons selectivity of 63% and C<sub>3</sub>H<sub>6</sub> selectivity of 10.2% were achieved. DFT calculations on LSCF and CoFe revealed that the high selectivity of the reduced in-situ LSCF for OCM arises primarily from CoFe nanoparticles. The elemental analysis on the surface and in the bulk of the LSCF and the reduced LSCF by XPS and XANES verified the reduced oxidation state of Co and Fe ions, including zerovalent species. The results of TPSR and insitu DRIFTS conducted under CH4 flow revealed that the reduced LSCF can successfully suppress deep oxidation of CH<sub>4</sub>, and that oxygen supply is an important parameter for selective conversion of CH4. The more basic surface of Red-LSCF than that of LSCF examined by In-situ TPD-DRIFTS using CO2 was also one of the key factors for the improved selectivity of C<sub>2+</sub> hydrocarbons from the electrocatalytic OCM.

#### CRediT authorship contribution statement

**Jaesung Kim**: Conceptualization, Investigation, Methodology, Data curation, Formal analysis, Writing – original draft. **Yu Jin Kim**: Investigation, Formal analysis, Writing – review & editing. **Matthew Ferree**: Investigation, Formal analysis, Writing – review & editing. **Seval** 

**Gunduz**: Investigation, Formal analysis, Writing – review & editing. **Minkyu Kim**: Investigation, Formal analysis, Writing – review & editing. **Anne C. Co**: Formal analysis, Writing – review. **Umit S. Ozkan**: Conceptualization, Funding acquisition, Project administration, Resources, Supervision, Formal analysis, Writing – review & editing.

#### **Declaration of Competing Interest**

The authors declare that they have no known competing financial interests or personal relationships that could have appeared to influence the work reported in this paper.

#### **Data Availability**

Data will be made available on request.

#### Acknowledgement

We would like to gratefully acknowledge the financial support provided for this work by the U.S. Department of Energy, Office of Science, Office of Basic Energy Sciences under the Award Number DE-FG02–07ER15896 and the U.S. National Science Foundation, under the award number 1932638. This research used resources of the Advanced Photon Source, a U.S. Department of Energy (DOE) Office of Science User Facility operated for the DOE Office of Science by Argonne National Laboratory under Contract No. DE-AC02–06CH11357. Electron microscopy was performed at the Center for Electron Microscopy and Analysis (CEMAS) at the Ohio State University. M.K. thanks support from National Research Foundation (NRF) of the Republic of Korea under the framework of Priority Research Centers Program funded by the Ministry of Education (2014R1A6A1031189) and Basic Science Research Program funded by the Ministry of Science, ICT, and Future Planning (2021R1C1C1004378).

#### Appendix A. Supporting information

Supplementary data associated with this article can be found in the online version at doi:10.1016/j.apcatb.2022.122026.

#### References

- E. McFarland, Unconventional chemistry for unconventional natural gas, Science 338 (2012) 340–342, https://doi.org/10.1126/science.12268.
- [2] P. Schwach, X. Pan, X. Bao, Direct conversion of methane to value-added chemicals over heterogeneous catalysts: challenges and prospects, Chem. Rev. 117 (2017) 8497–8520, https://doi.org/10.1021/acs.chemrev.6b00715.
- [3] P. Schwach, N. Hamilton, M. Eichelbaum, L. Thum, T. Lunkenbein, R. Schlögl, A. Trunschke, Structure sensitivity of the oxidative activation of methane over MgO model catalysts: II. Nature of active sites and reaction mechanism, J. Catal. 329 (2015) 574–587, https://doi.org/10.1016/j.jcat.2015.05.008.
- [4] B.L. Farrell, V.O. Igenegbai, S. Linic, A viewpoint on direct methane conversion to ethane and ethylene using oxidative coupling on solid catalysts, ACS Catal. 6 (2016) 4340–4346, https://doi.org/10.1021/acscatal.6b01087.
- [5] Y.S. Su, J.Y. Ying, W.H. Green Jr, Upper bound on the yield for oxidative coupling of methane, J. Catal. 218 (2003) 321–333, https://doi.org/10.1016/S0021-9517 (03)00043-5.
- [6] Z. Stansch, L. Mleczko, M. Baerns, Comprehensive kinetics of oxidative coupling of methane over the La<sub>2</sub>O<sub>3</sub>/CaO catalyst, Ind. Eng. Chem. Res. 36 (1997) 2568–2579, https://doi.org/10.1021/ie960562k.
- [7] C. Zhu, S. Hou, X. Hu, J. Lu, F. Chen, K. Xie, Electrochemical conversion of methane to ethylene in a solid oxide electrolyzer, Nat. Commun. 10 (2019) 1173, https://doi.org/10.1038/s41467-019-09083-3.
- [8] K. Liu, J. Zhao, D. Zhu, F. Meng, F. Kong, Y. Tang, Oxidative coupling of methane in solid oxide fuel cell tubular membrane reactor with high ethylene yield, Catal. Commun. 96 (2017) 23–27. https://doi.org/10.1016/j.catcom.2017.03.010.
- [9] S.A. Venâncio, P.E.V. de Miranda, Direct utilization of carbonaceous fuels in multifunctional SOFC anodes for the electrosynthesis of chemicals or the generation of electricity, Inter. J. Hydrog. Ener 42 (2017) 13927–13938, https:// doi.org/10.1016/j.ijhydene.2017.02.051.
- [10] D.J. Deka, J. Kim, S. Gunduz, M. Aouine, J.-M.M. Millet, A.C. Co, U.S. Ozkan, Investigation of hetero-phases grown via in-situ exsolution on a Ni-doped (La,Sr) FeO<sub>3</sub> cathode and the resultant activity enhancement in CO<sub>2</sub> reduction, Appl. Catal. B 286 (2021), 119917, https://doi.org/10.1016/j.apcatb.2021.119917.

- [11] D.J. Deka, S. Gunduz, T. Fitzgerald, J.T. Miller, A.C. Co, U.S. Ozkan, Production of syngas with controllable H<sub>2</sub>/CO ratio by high temperature co-electrolysis of CO<sub>2</sub> and H<sub>2</sub>O over Ni and Co- doped lanthanum strontium ferrite perovskite cathodes, Appl. Catal. B 248 (2019) 487–503, https://doi.org/10.1016/j. apcatb.2019.02.045.
- [12] B.H. Toby, R.B.Von Dreele, GSAS-II: the genesis of a modern open-source all purpose crystallography software package, J. Appl. Crystallogr. 46 (2013) 544–549, https://doi.org/10.1107/S0021889813003531.
- [13] S.-K. Otto, K. Kousi, D. Neagu, L. Bekris, J. Janek, I.S. Metcalfe, Exsolved nickel nanoparticles acting as oxygen storage reservoirs and active sites for redox CH<sub>4</sub> conversion, ACS Appl. Energy Mater. 2 (2019) 7288–7298, https://doi.org/ 10.1021/acsaem.9b01267
- [14] K. Momma, F. Izumi, VESTA3for three-dimensional visualization of crystal, volumetric and morphology data, J. Appl. Crystallogr. 44 (2011) 1272–1276, https://doi.org/10.1107/S0021889811038970.
- [15] B. Ravel, M. Newville, Athena, artemis, hephaestus: data analysis for X-ray absorption spectroscopy using IFEFFIT, J. Synchrotron Radiat. 12 (2005) 537–541, https://doi.org/10.1107/S0909049505012719.
- [16] P.E. Blochl, Projector augmented-wave method, Phys. Rev. B Condens. Matter 50 (1994) 17953–17979, https://doi.org/10.1103/PhysRevB.50.17953.
- [17] G. Kresse, J. Hafner, Ab initio Hellmann-Feynman molecular dynamics for liquid metals, J. Non-Cryst. Solids.: X (1993) 956–960, https://doi.org/10.1016/0022-3093(93)90104-6.
- [18] A.M. Ritzmann, J.M. Dieterich, E.A. Carter, Density functional theory + U analysis of the electronic structure and defect chemistry of LSCF (La<sub>0.5</sub>Sr<sub>0.5</sub>Co<sub>0.25</sub>Fe<sub>0.75</sub>O<sub>3-8</sub>), Phys. Chem. Chem. Phys. 18 (2016) 12260–12269, https://doi.org/10.1039/ C6CP01720G.
- [19] Y. Yu, H. Luo, D. Cetin, X. Lin, K. Ludwig, U. Pal, S. Gopalan, S. Basu, Effect of atmospheric CO<sub>2</sub> on surface segregation and phase formation in La<sub>0.6</sub>Sr<sub>0.4</sub>Co<sub>0.2</sub>Fe<sub>0.8</sub>O<sub>3-8</sub> thin films, Appl. Surf. Sci. 323 (2014) 71–77, https://doi. org/10.1016/j.apsusc.2014.09.019.
- [20] P. Rochana, J. Wilcox, A theoretical study of CO adsorption on FeCo(100) and the effect of alloying, Surf. Sci. 605 (2011) 681–688, https://doi.org/10.1016/j. susc.2011.01.003.
- [21] M.S.D. Read, M. Saiful Islam, G.W. Watson, F. King, F.E. Hancock, Defect chemistry and surface properties of LaCoO<sub>3</sub>, J. Mater. Chem. 10 (2000) 2298–2305, https://doi.org/10.1039/B002168G.
- [22] J.K. Nørskov, J. Rossmeisl, A. Logadottir, L. Lindqvist, Origin of the overpotential for oxygen reduction at a fuel-cell cathode, J. Phys. Chem. B (2004) 17886–17892, https://doi.org/10.1021/jp047349j.
- [23] K.-Y. Lai, A. Manthiram, Evolution of exsolved nanoparticles on a perovskite oxide surface during a redox process, Chem. Mater. 30 (2018) 2838–2847, https://doi. org/10.1021/acs.chemmater.8b01029.
- [24] B. Jin, Z. Shang, S. Li, Y.-B. Jiang, X. Gu, X. Liang, Reforming of methane with carbon dioxide over cerium oxide promoted nickel nanoparticles deposited on 4channel hollow fibers by atomic layer deposition, Catal. Sci. Technol. 10 (2020) 3212–3222, https://doi.org/10.1039/D0CY00039F.
- [25] D. Zubenko, S. Singh, B.A. Rosen, Exsolution of Re-alloy catalysts with enhanced stability for methane dry reforming, Appl. Catal. B 209 (2017) 711–719, https:// doi.org/10.1016/j.apcatb.2017.03.047.
- [26] N. Shi, S. Xue, Y. Xie, Y. Yang, D. Huan, Y. Pan, R. Peng, C. Xia, Z. Zhan, Y. Lu, Co-generation of electricity and olefin via proton conducting fuel cells using (Pr<sub>0.3</sub>Sr<sub>0.7</sub>)<sub>0.9</sub>Ni<sub>0.1</sub>Ti<sub>0.9</sub>O<sub>3</sub> catalyst layers, Appl. Catal. B 272 (2020), 118973, https://doi.org/10.1016/j.apcatb.2020.118973.
- [27] G. Nirala, D. Yadav, S. Upadhyay, Ruddlesden-Popper phase A<sub>2</sub>BO<sub>4</sub> oxides: recent studies on structure, electrical, dielectric, and optical properties, J. Adv. Ceram. 9 (2020) 129–148, https://doi.org/10.1007/s40145-020-0365-x.
- [28] D. Neagu, G. Tsekouras, D.N. Miller, H. Menard, J.T. Irvine, In situ growth of nanoparticles through control of non-stoichiometry, Nat. Chem. 5 (2013) 916–923, https://doi.org/10.1038/nchem.1773.
- [29] J. Kiwi, K.R. Thampi, N. Mouaddib, M. Grätzel, Oxidative coupling of methane. The effect of alkali chlorides on molybdate based catalyst leading to high selectivity in C<sub>3</sub>-product formation, J. Catal. 18 (1993) 15–26, https://doi.org/ 10.1007/BF00769494.
- [30] D. Noon, B. Zohour, S. Senkan, Oxidative coupling of methane with La<sub>2</sub>O<sub>3</sub>–CeO<sub>2</sub> nanofiber fabrics: a reaction engineering study, J. Nat. Gas. Sci. Eng. 18 (2014) 406–411, https://doi.org/10.1016/j.jngse.2014.04.004.
- [31] T. Li, M. Kim, R. Rai, Z. Liang, A. Asthagiri, J.F. Weaver, Adsorption of alkanes on stoichiometric and oxygen-rich RuO<sub>2</sub>(110), Phys. Chem. Chem. Phys. 18 (2016) 22647–22660, https://doi.org/10.1039/C6CP04195G.
- [32] R. Martin, M. Kim, A. Asthagiri, J.F. Weaver, Alkane activation and oxidation on late-transition-metal oxides: challenges and opportunities, ACS Catal. 11 (2021) 4682, https://doi.org/10.1021/acscatal.1c00612.
- [33] J. Kuhn, U. Ozkan, Surface properties of Sr- and Co-doped LaFeO<sub>3</sub>, J. Catal. 253 (2008) 200–211, https://doi.org/10.1016/j.jcat.2007.10.005.
- [34] S. Maity, S.K. Ray, D. Bhattacharya, Phase, morphology and core-level electron spectroscopy of nano-sized La<sub>0.65</sub>Sr<sub>0.35</sub>MnO<sub>3</sub> powders prepared by solution combustion synthesis, J. Phys. Chem. Solids 74 (2013) 315–321, https://doi.org/ 10.1016/j.jpcs.2012.10.006.
- [35] R.C. Schucker, K.J. Derrickson, A.K. Ali, N.J. Caton, The effect of strontium content on the activity and selectivity of Sr-doped La<sub>2</sub>O<sub>3</sub> catalysts in oxidative coupling of methane, Appl. Catal. A 607 (2020) 11397–11404, https://doi.org/10.1016/j. apcata.2020.117827.
- [36] S.B. Hammouda, F. Zhao, Z. Safaei, V. Srivastava, D. Lakshmi Ramasamy, S. Iftekhar, S. kalliola, M. Sillanpää, Degradation and mineralization of phenol in aqueous medium by heterogeneous monopersulfate activation on nanostructured

- cobalt based-perovskite catalysts ACoO $_3$  (A = La, Ba, Sr and Ce): characterization, kinetics and mechanism study, Appl. Catal. B 215 (2017) 60–73, https://doi.org/10.1016/j.apcatb.2017.05.051.
- [37] M. Descostes, F. Mercier, N. Thromat, C. Beaucaire, M. Gautier-Soyer, Use of XPS in the determination of chemical environment and oxidation state of iron and sulfur samples: constitution of a data basis in binding energies for Fe and S reference compounds and applications to the evidence of surface species of an oxidized pyrite in a carbonate medium, Appl. Surf. Sci. 165 (2000) 288–302, https://doi.org/ 10.1016/S0169-4332(00)00443-8.
- [38] B. Niu, C. Lu, W. Yi, S. Luo, X. Li, X. Zhong, X. Zhao, B. Xu, In-situ growth of nanoparticles-decorated double perovskite electrode materials for symmetrical solid oxide cells, Appl. Catal. B 270 (2020) 1427–1438, https://doi.org/10.1016/j. apcatb.2020.118842.
- [39] J.W. Stevenson, T.R. Armstrong, R.D. Carneim, L.R. Pederson, W.J. Weber, Electrochemical properties of mixed conducting perovskites La<sub>1-x</sub>MxCo<sub>1-y</sub>FeyO<sub>3-8</sub> (M=Sr, Ba, Ca), J. Electrochem. Soc. 143 (1996) 2722–2729, https://doi.org/ 10.1149/1.1837098.
- [40] N. Lakshminarayanan, H. Choi, J.N. Kuhn, U.S. Ozkan, Effect of additional B-site transition metal doping on oxygen transport and activation characteristics in La<sub>0.6</sub>Sr<sub>0.4</sub>(Co<sub>0.18</sub>Fe<sub>0.72</sub>X<sub>0.1</sub>)O<sub>3-6</sub> (where X—Zn, Ni or Cu) perovskite oxides, Appl. Catal. B 103 (2011) 318–325, https://doi.org/10.1016/j.apcatb.2011.01.038.
- [41] T. Gholam, L.R. Zheng, J.O. Wang, H.J. Qian, R. Wu, H.Q. Wang, Synchrotron X-ray absorption spectroscopy study of local structure in Al-Doped BiFeO<sub>3</sub> powders, Nanoscale. Res. Lett. 14 (2019) 137, https://doi.org/10.1186/s11671-019-2965-3.
- [42] O. Haas, U.F. Vogt, C. Soltmann, A. Braun, W.S. Yoon, X.Q. Yang, T. Graule, The Fe K-edge X-ray absorption characteristics of La<sub>1-x</sub>Sr<sub>x</sub>FeO<sub>3-8</sub> prepared by solid state reaction, Mater. Res. Bull. 44 (2009) 1397–1404, https://doi.org/10.1016/j.materresbull.2008.11.026.
- [43] D. Dogu, S. Gunduz, K.E. Meyer, D.J. Deka, A.C. Co, U.S. Ozkan, CO<sub>2</sub> and H<sub>2</sub>O electrolysis using solid oxide electrolyzer cell (SOEC) with La and Cl- doped strontium titanate cathode, Catal. Lett. 149 (2019) 1743–1752, https://doi.org/10.1007/s10562-019-02786-8.
- [44] T. Zhang, W. Wang, F. Gu, W. Xu, J. Zhang, Z. Li, T. Zhu, G. Xu, Z. Zhong, F. Su, Enhancing the low-temperature CO<sub>2</sub> methanation over Ni/La-CeO<sub>2</sub> catalyst: the effects of surface oxygen vacancy and basic site on the catalytic performance, Appl. Catal. B 312 (2022), 121385, https://doi.org/10.1016/j.apcatb.2022.121385.
- [45] G. Karamullaoglu, T. Dogu, Oxidative dehydrogenation of ethane over a monolith coated by molybdenum-vanadium-niobium mixed-oxide catalyst, Chem. 1 Eng. Commun. 190 (2010) 1427–1438, https://doi.org/10.1080/00986440302149.
- [46] A. Litke, Y. Su, I. Tranca, T. Weber, E.J.M. Hensen, J.P. Hofmann, Role of adsorbed water on charge carrier dynamics in photoexcited TiO<sub>2</sub>, J. Phys. Chem. C.

- Nanomater Interfaces 121 (2017) 7514–7524, https://doi.org/10.1021/acs.incc.7b00472.
- [47] M.D. Driessen, V.H. Grassian, Methyl Spillover on Silica-Supported Copper Catalysts from the Dissociative Adsorption of Methyl Halides, J. Catal. 161 (1996) 810–818, https://doi.org/10.1006/jcat.1996.0244.
- [48] X. Xiao, J. Gao, S. Xi, S.H. Lim, A.K.W. Png, A. Borgna, W. Chu, Y. Liu, Experimental and in situ DRIFTs studies on confined metallic copper stabilized Pd species for enhanced CO<sub>2</sub> reduction to formate, Appl. Catal. B 309 (2022), 121239, https://doi.org/10.1016/j.apcatb.2022.121239.
- [49] U. Zavyalova, M. Holena, R. Schlögl, M. Baerns, Statistical analysis of past catalytic data on oxidative methane coupling for new insights into the composition of highperformance catalysts, ChemCatChem 3 (2011) 1935–1947, https://doi.org/ 10.1002/cctc.201100186.
- [50] X. Li, Z.J. Zhao, L. Zeng, J. Zhao, H. Tian, S. Chen, K. Li, S. Sang, J. Gong, On the role of Ce in  $\rm CO_2$  adsorption and activation over lanthanum species, Chem. Sci. 9 (2018) 3426–3437, https://doi.org/10.1039/C8SC00203G.
- [51] V. Kharton, E. Tsipis, I. Marozau, A. Viskup, J. Frade, J. Irvine, Mixed conductivity and electrochemical behavior of (La<sub>0.75</sub>Sr<sub>0.25</sub>)<sub>0.95</sub>Cr<sub>0.5</sub>Mn<sub>0.5</sub>O<sub>3-6</sub>, Solid State Ion. 178 (2007) 101–113, https://doi.org/10.1016/j.ssi.2006.11.012.
- [52] S. Yu, D. Yoon, Y. Lee, H. Yoon, H. Han, N. Kim, C.J. Kim, K. Ihm, T.S. Oh, J. Son, Metal nanoparticle exsolution on a perovskite stannate support with high electrical conductivity, Nano. Lett. 20 (2020) 3538–3544, https://doi.org/10.1021/acs. nanolett.0c00488.
- [53] D.J. Deka, J. Kim, S. Gunduz, M. Ferree, A.C. Co, U.S. Ozkan, Temperature-induced changes in the synthesis gas composition in a high-temperature H<sub>2</sub>O and CO<sub>2</sub> coelectrolysis system, Appl. Catal. A 602 (2020), 117697, https://doi.org/10.1016/j. apcata.2020.117697.
- [54] A. Nenning, A.K. Opitz, C. Rameshan, R. Rameshan, R. Blume, M. Havecker, A. Knop-Gericke, G. Rupprechter, B. Klotzer, J. Fleig, Ambient pressure XPS study of mixed conducting perovskite-Type SOFC cathode and anode materials under well-defined electrochemical polarization, J. Phys. Chem. C. Nanomater Interfaces 120 (2016) 1461–1471, https://doi.org/10.1021/acs.jpcc.5b08596.
- [55] D.N. Mueller, M.L. Machala, H. Bluhm, W.C. Chueh, Redox activity of surface oxygen anions in oxygen-deficient perovskite oxides during electrochemical reactions, Nat. Commun. 6 (2015) 6097, https://doi.org/10.1038/ncomms7097
- [56] B.F. Serodio Costa, B.I. Arias-Serrano, A.A. Yaremchenko, Development of Ni-Sr(V, Ti)O3-delta fuel electrodes for solid oxide fuel cells, Mater. (Basel) 15 (2021) 278, https://doi.org/10.3390/ma15010278.
- [57] Z. Du, H. Zhao, S. Yi, Q. Xia, Y. Gong, Y. Zhang, X. Cheng, Y. Li, L. Gu, K. Swierczek, High-performance anode material Sr<sub>2</sub>FeMo<sub>0.65</sub>Ni<sub>0.35</sub>O<sub>6-8</sub> with in situ exsolved nanoparticle catalyst, ACS Nano 10 (2016) 8660–8669, https://doi.org/ 10.1021/acsnano.6b03979.